This is a preprint of an article accepted for publication in Journal of Cold Regions Science and Technology on 17 December 2012. The published article is available online at http://www.sciencedirect.com/science/article/pii/S0165232X12002480
To be cited as: Goulmot D., Bouaanani N. 2013. Seismic analysis of rectangular water-containing structures with floating ice blocks. Journal of Cold Regions Science and Technology, 90-91: 22–32.

Seismic Analysis of Rectangular Water-Containing Structures with Floating Ice Blocks

Damien Goulmot [1] and Najib Bouaanani [2]

ABSTRACT

This paper presents a new formulation to investigate the effects of floating ice blocks on seismically-excited rectangular water-containing structures. The proposed method is based on a sub-structuring approach, where the flexible containing structure and ice-added mass are modeled using finite elements, while hydrodynamic effects are modeled analytically through interaction forces at the water-structure and water-ice interfaces, thus eliminating the need for reservoir finite element discretization. In addition to accounting for the influence of floating ice blocks and container walls' flexibility, the developed frequency- and time-domain techniques also include the effects of container geometrical or material asymmetry as well as the coupling between convective and impulsive components of hydrodynamic pressure. The proposed formulation is illustrated through a numerical example illustrating the dynamic response of symmetric and asymmetric water-containing structures covered with floating ice blocks. Obtained time- and frequency-domain responses are successfully validated against advanced finite element analyses including fluid-structure interaction capabilities. For the water-containing structures studied, the results show that the presence of floating ice blocks affects the frequency content and amplitudes of the dynamic responses corresponding to convective and impulsive modes.

Key words: Dynamic response; Water-containing structure; Ice effects; Floating ice blocks; Sloshing ice; Hydrodynamic pressure.

[1] Graduate Research Assistant, Department of Civil, Geological and Mining Engineering,
École Polytechnique de Montréal, Montréal, QC H3C 3A7, Canada.
[2] Professor, Department of Civil, Geological and Mining Engineering,
École Polytechnique de Montréal, Montréal, QC H3C 3A7, Canada
Corresponding author. E-mail: najib.bouaanani@polymtl.ca

1 Introduction

The dynamic behavior of water-containing structures has been widely studied in the last five decades to predict their response to seismic excitations and prevent heavy damage as observed during the 1960 Chilean Earthquakes (Steinbrugge and Flores, 1963), the 1964 Alaska Earthquake (Hanson, 1973), and more recently the 1994 Northridge Earthquake (Hall, 1995), the 1999 Turkey Earthquake (Steinberg and Cruz, 2004) and the 2003 Tokachi-oki Earthquake (Koketsu et al., 2005).

In earlier analytical work, the containing structure was assumed rigid and the studies mainly focused on the dynamic behavior of the contained liquid (Jacobsen, 1949; Werner and Sundquit, 1949; Jacobsen and Ayre, 1951; Housner, 1957; Housner, 1963). Significant observed post-earthquake damage showed that the rigid assumption may lead to the underestimation of the seismic response of such structures, and clearly indicated the necessity of including the flexibility and vibrating response of the containing structure as well as its coupled interaction with the contained liquid.

The work of Chopra (1967, 1968, 1970), Veletsos (1974), Haroun (1980) and many others subsequently (Veletsos and Yang, 1976; Veletsos and Yang, 1977; Haroun and Housner, 1981a; Haroun and Housner, 1981b; Haroun, 1983; Balendra et al., 1982), confirmed that structural flexibility affects considerably the coupled dynamic response of water-containing structures. Another phenomenon which attracted the attention of many researchers is the effect of surface gravity waves and corresponding sloshing at the surface of the contained liquid during earthquake excitation. Indeed, it has been evidenced that liquid sloshing was generally a source of most damage observed in the upper part of liquid containing structures (Krausmann et al., 2011). In numerical analyses, dynamic fluid pressures are generally decomposed into (i) a convective component generated by the sloshing of a portion of the fluid near the surface, and (ii) an impulsive component generated by a portion of the fluid accelerating with the containing structure. It has been shown that the coupling between liquid sloshing modes and container vibration modes is generally weak (Veletsos, 1974; Haroun, 1980; Haroun and Housner, 1982). Convective and impulsive pressures can then be first determined separately and their effects combined later to obtain the total dynamic response (Kana, 1979; Malhotra et al., 2000). Several researchers proposed refined analytical and numerical methods to assess sloshing effects in seismically-excited tanks, such as Veletsos and Tang (1976), Gupta and Hutchinson (1990), Fisher and Rammerstorfer (1999), and Ghaemmaghami and Kianoush (2010).

In cold climates, water-containing structures such as dams, tanks or navigation locks are generally covered with 1 to $2\,$m-thick ice sheets for significant periods of time during the year. Increasing exploration of natural ressources in northern regions has motivated a variety of research programs which mainly focused on the dynamic response of ice-surrounded offshore platforms to drifting ice action as well as to seismic excitation (Cammaert and Muggeridge, 1988; Croteau, 1983; Miura et al., 1988; Sun, 1993; Kiyokawa and Inada, 1989). Forced vibration tests were carried out on a large gravity dam in Quebec under both summer and severe winter conditions including the presence of an ice cover (Paultre et al., 2002). The experimental results and subsequent numerical studies have shown that the ice cover affects the dynamic response of gravity dams as well as hydrodynamic pressure distribution in the reservoir (Bouaanani et al., 2002). In all previous studies, the ice-covered water domain was assumed infinite, or delimited at a given truncating distance from the structure by a transmitting boundary condition to account for energy radiation at infinity (Bouaanani and Paultre, 2005). However, the dynamic or seismic response of ice-covered water reservoirs of limited extent such as water storages, channels and navigation locks received almost no attention in the literature.

In this paper, we investigate the effect of floating ice blocks on the dynamic characteristics and seismic response of rectangular water-containing structures such as the one illustrated in Fig. 1. The dynamic analysis of such systems, commonly encountered in cold regions, requires the modeling of simultaneous dynamic interactions between floating ice blocks, water and the containing structure. The analytical method developed in this work will address the dynamic and seismic behavior of such systems using a sub-structuring technique where structural and hydrodynamic responses are coupled through interface forces. Finite element modeling is then restricted to the containing structure, while hydrodynamic effects are accounted for analytically, thus eliminating the need for reservoir finite element discretization. In addition to accounting for the influence of floating ice blocks and container walls' flexibility, the developed frequency- and time-domain techniques will also include the effects of possible geometrical or material asymmetry of the containing structure as well as the coupling between convective and impulsive components of hydrodynamic pressure.

2 Mathematical formulation

2.1 General assumptions and governing equations

We consider a rectangular water-containing structure as the one depicted in Fig. 1. We assume that: (i) the longitudinal dimensions of the structure are sufficiently large so that it can be modeled as a two-dimensional plane-strain elasticity problem, (ii) the constitutive material of the containing structure has a linear elastic behavior, (iii) the lateral walls of the containing structure are flexible and have vertical faces at the interfaces with the reservoir, (iv) water is compressible, inviscid, with its motions irrotational and limited to small amplitudes, (v) water surface is covered by floating ice blocks, vibrating vertically without friction, and (iv) the containing-structure can be geometrically or materially asymmetrical.

The reservoir has a length $L_{\mathrm{r}} = 2b_{\mathrm{r}}$ and height H_{r} as indicated in Fig. 1. We adopt a Cartesian coordinate system with origin at the reservoir bottom, a horizontal axis x and a vertical axis y coincident with the axis of symmetry of the reservoir. As mentioned previously, we will apply a sub-structuring approach as illustrated in Fig. 2, where the flexible containing structure and ice-added mass are modeled using finite elements, while water effects are modeled analytically through interaction forces at the water-structure and water-ice interfaces.

The hydrodynamic pressure $p(x, y, t)$ within the reservoir is governed by the classical wave equation

$$\nabla^2 p = \frac{1}{C_{\mathrm{r}}^2} \frac{\partial^2 p}{\partial t^2} \tag{1}$$

where ∇^2 is the Laplace differential operator, t the time variable, ρ_{r} the mass density of water and C_{r} the compression wave velocity. We consider harmonic ground accelerations $\ddot{u}_{\mathrm{g}}(t) = a_{\mathrm{g}}\, \mathrm{e}^{i\omega t}$ where ω denotes the exciting frequency. Hydrodynamic pressure in the reservoir can then be expressed in frequency domain as $\bar{p}(x, y, t) = \bar{p}(x, y, \omega)\, \mathrm{e}^{i\omega t}$, where $\bar{p}(x, y, \omega)$ is a complex-valued frequency response function (FRF). Eq. (1) becomes then the classical Helmholtz equation

$$\nabla^2 \bar{p} + \frac{\omega^2}{C_{\mathrm{r}}^2}\, \bar{p} = 0 \tag{2}$$

Using a modal superposition analysis, the FRFs for structural displacements and accelerations can be expressed as

$$\bar{u}(x, y, \omega) = \sum_{j=1}^{m_{\mathrm{s}}} \psi_j^{(x)}(x, y) \bar{Z}_j(\omega)\,; \qquad \bar{v}(x, y, \omega) = \sum_{j=1}^{m_{\mathrm{s}}} \psi_j^{(y)}(x, y) \bar{Z}_j(\omega) \tag{3}$$

$$\bar{\ddot{u}}(x, y, \omega) = -\omega^2 \sum_{j=1}^{m_{\mathrm{s}}} \psi_j^{(x)}(x, y) \bar{Z}_j(\omega)\,; \qquad \bar{\ddot{v}}(x, y, \omega) = -\omega^2 \sum_{j=1}^{m_{\mathrm{s}}} \psi_j^{(y)}(x, y) \bar{Z}_j(\omega) \tag{4}$$

where $\bar{u}$ and $\bar{v}$ denote the horizontal and vertical displacements, respectively, $\bar{\ddot{u}}$ and $\bar{\ddot{v}}$ the horizontal and vertical accelerations, respectively, $\psi_j^{(x)}$ and $\psi_j^{(y)}$ the x- and y-components of the j th structural mode shape, respectively, $\bar{Z}_j$ the generalized coordinate, and m_{s} the number of structural mode shapes included in the analysis. The FRF $\bar{p}$ for hydrodynamic pressure can be written as (Fenves and Chopra, 1984; Bouaanani and Lu, 2009)

$$\bar{p}(x, y, \omega) = \bar{p}_0(x, y, \omega) - \omega^2 \sum_{j=1}^{m_{\mathrm{s}}} \bar{Z}_j(\omega)\, \bar{p}_j(x, y, \omega) \tag{5}$$

where $\bar{p}_0$ is the FRF for hydrodynamic pressure due to rigid body motion of the containing structure subjected to ground acceleration $\bar{\ddot{u}}_{\mathrm{g}}$, and where $\bar{p}_j$ is the FRF for hydrodynamic pressure due to horizontal ground accelerations $\psi_j^{(x)}(-b_{\mathrm{r}}, y)$ and $\psi_j^{(x)}(b_{\mathrm{r}}, y)$ of the lateral walls of the containing structure vibrating along structural mode j. Hydrodynamic pressure FRF $\bar{p}$ can be decomposed into an impulsive component $\bar{p}_{\mathrm{I}}$ and a convective component $\bar{p}_{\mathrm{C}}$, yielding

$$\begin{aligned} \bar{p}(x, y, \omega) &= \bar{p}_{\mathrm{I}}(x, y, \omega) + \bar{p}_{\mathrm{C}}(x, y, \omega) \\ &= \bar{p}_{\mathrm{I},0}(x, y, \omega) + \bar{p}_{\mathrm{C},0}(x, y, \omega) \\ &\quad - \omega^2 \sum_{j=1}^{m_{\mathrm{s}}} \Big[\bar{p}_{\mathrm{I},j}(x, y, \omega) + \bar{p}_{\mathrm{C},j}(x, y, \omega)\Big] \bar{Z}_j(\omega) \end{aligned} \tag{6}$$

The boundary conditions to be satisfied by FRFs $\bar{p}_{\mathrm{I},0}$, $\bar{p}_{\mathrm{C},0}$, $\bar{p}_{\mathrm{I},j}$ and $\bar{p}_{\mathrm{C},j}$ are as follows

– *At structure-reservoir vertical interfaces*

$$\frac{\partial \bar{p}_{\mathrm{I},0}}{\partial x}(\pm b_{\mathrm{r}}, y, \omega) = -\rho_{\mathrm{r}} \bar{\ddot{u}}_{\mathrm{g}}(\omega)\,; \qquad \frac{\partial \bar{p}_{\mathrm{C},0}}{\partial x}(\pm b_{\mathrm{r}}, y, \omega) = 0 \tag{7}$$

$$\frac{\partial \bar{p}_{\mathrm{I},j}}{\partial x}(\pm b_{\mathrm{r}}, y, \omega) = -\rho_{\mathrm{r}} \psi_j(\pm b_{\mathrm{r}}, y)\,; \qquad \frac{\partial \bar{p}_{\mathrm{C},j}}{\partial x}(\pm b_{\mathrm{r}}, y, \omega) = 0 \tag{8}$$

– *At reservoir bottom*

$$\frac{\partial \bar{p}_{\mathrm{I},0}}{\partial y}(x, 0, \omega) = 0\,; \qquad \frac{\partial \bar{p}_{\mathrm{C},0}}{\partial y}(x, 0, \omega) = 0 \tag{9}$$

$$\frac{\partial \bar{p}_{\mathrm{I},j}}{\partial y}(x, 0, \omega) = 0\,; \qquad \frac{\partial \bar{p}_{\mathrm{C},j}}{\partial y}(x, 0, \omega) = 0 \tag{10}$$

– *At reservoir surface*

$$\left(\rho_{\mathrm{r}} g - \rho_{\mathrm{i}} h_{\mathrm{i}}\, \omega^2\right) \frac{\partial \bar{p}}{\partial y}(x, H_{\mathrm{r}}, \omega) = \rho_{\mathrm{r}} \omega^2 \bar{p}(x, H_{\mathrm{r}}, \omega) \tag{11}$$

$$\bar{p}_{I,0}(x, H_{\mathrm{r}}, \omega) = \bar{p}_{I,j}(x, H_{\mathrm{r}}, \omega) = 0 \tag{12}$$

where ρ_{i} denotes the mass density of floating ice blocks, h_{i} their average thickness and g the acceleration due to gravity. The boundary condition in Eq. (11) was derived using the kinematic condition and linearized Bernoulli's equation at the interface between the floating ice blocks and the reservoir (Weitz and Keller, 1950; Sun, 1993; Bouaanani et al., 2002). Adopting the decomposition of hydrodynamic pressure into a convective and an impulsive pressure as per Eq. (6), and substituting Eq. (12) into Eq. (11), the surface boundary condition in Eq. (11) yields the two following boundary conditions expressed in terms of FRFs $\bar{p}_{\mathrm{I},0}$, $\bar{p}_{\mathrm{C},0}$, $\bar{p}_{\mathrm{I},j}$ and $\bar{p}_{\mathrm{C},j}$, $j = 1 \ldots m_{\mathrm{s}}$

$$\left(\rho_{\mathrm{r}} g - \rho_{\mathrm{i}} h_{\mathrm{i}}\, \omega^2\right) \frac{\partial \bar{p}_{\mathrm{C},0}}{\partial y}(x, H_{\mathrm{r}}, \omega) - \rho_{\mathrm{r}} \omega^2 \bar{p}_{\mathrm{C},0}(x, H_{\mathrm{r}}, \omega) = -\left(\rho_{\mathrm{r}} g - \rho_{\mathrm{i}} h_{\mathrm{i}}\, \omega^2\right) \frac{\partial \bar{p}_{\mathrm{I},0}}{\partial y}(x, H_{\mathrm{r}}, \omega) \tag{13}$$

$$\left(\rho_{\mathrm{r}} g - \rho_{\mathrm{i}} h_{\mathrm{i}}\, \omega^2\right) \frac{\partial \bar{p}_{\mathrm{C},j}}{\partial y}(x, H_{\mathrm{r}}, \omega) - \rho_{\mathrm{r}} \omega^2 \bar{p}_{\mathrm{C},j}(x, H_{\mathrm{r}}, \omega) = -\left(\rho_{\mathrm{r}} g - \rho_{\mathrm{i}} h_{\mathrm{i}}\, \omega^2\right) \frac{\partial \bar{p}_{\mathrm{I},j}}{\partial y}(x, H_{\mathrm{r}}, \omega) \tag{14}$$

The FRF $\bar{p}$ for total hydrodynamic pressure is given by Eq. (6) where the vector $\bar{\mathbf{Z}}$ of generalized coordinates $\bar{Z}_j$, $j = 1 \ldots m_{\mathrm{s}}$, is obtained by solving the system of equations

$$\bar{\mathbf{S}}\, \bar{\mathbf{Z}} = \bar{\mathbf{Q}} \tag{15}$$

in which elements of matrices $\bar{\mathbf{S}}$ and $\bar{\mathbf{Q}}$ are obtained for $n=1\dots m_\mathrm{s}$ and $j=1\dots m_\mathrm{s}$ as

$$\begin{aligned}\bar{S}_{nj}(\omega) =& \Big[-\omega^2+\Big(1+\mathrm{i}\,\eta_\mathrm{s}\Big)\,\omega_n^2\Big]\delta_{nj}\\ &+\omega^2\Bigg\{\int_0^{H_\mathrm{r}}\Big[\bar{p}_{\mathrm{I},j}(b_\mathrm{r},y,\omega)+\bar{p}_{\mathrm{C},j}(b_\mathrm{r},y,\omega)\Big]\,\psi_n^{(x)}(b_\mathrm{r},y)\,\mathrm{d}y\\ &\qquad-\int_0^{H_\mathrm{r}}\Big[\bar{p}_{\mathrm{I},j}(-b_\mathrm{r},y,\omega)+\bar{p}_{\mathrm{C},j}(-b_\mathrm{r},y,\omega)\Big]\,\psi_n^{(x)}(-b_\mathrm{r},y)\,\mathrm{d}y\Bigg\}\end{aligned}\tag{16}$$

$$\begin{aligned}\bar{Q}_n(\omega) =& -\boldsymbol{\psi}_n^\mathrm{T}\,\mathbf{M}\,\mathbf{1}+\int_0^{H_\mathrm{r}}\Big[\bar{p}_{\mathrm{I},0}(b_\mathrm{r},y,\omega)+\bar{p}_{\mathrm{C},0}(b_\mathrm{r},y,\omega)\Big]\,\psi_n^{(x)}(b_\mathrm{r},y)\,\mathrm{d}y\\ &-\int_0^{H_\mathrm{r}}\Big[\bar{p}_{\mathrm{I},0}(-b_\mathrm{r},y,\omega)+\bar{p}_{\mathrm{C},0}(-b_\mathrm{r},y,\omega)\Big]\,\psi_n^{(x)}(-b_\mathrm{r},y)\,\mathrm{d}y\end{aligned}\tag{17}$$

where δ denotes the Kronecker symbol, ω_n is the vibration frequency corresponding to structural mode shape $\boldsymbol{\psi}_n$ of the empty containing structure combined to ice-added mass, $\mathbf{M}$ is the mass matrix of the ice-container system, η_s is the structural hysteretic damping factor, and $\mathbf{1}$ is a column-vector with the same dimension as the vector of nodal relative displacements, containing zeros except along horizontal degrees of freedom which correspond to the direction of earthquake excitation.

2.2 Impulsive hydrodynamic pressure

Solutions for FRFs $\bar{p}_{\mathrm{I},0}$ and $\bar{p}_{\mathrm{I},j}$, $j=1\dots m_\mathrm{s}$, are developed next using Eq. (2), and the associated boundary conditions described in the previous section. Considering a unit horizontal ground acceleration $\bar{\ddot{u}}_\mathrm{g}(\omega)=1$, we show in Appendix A that FRF $\bar{p}_{\mathrm{I},0}$ can be expressed as

$$\bar{p}_{\mathrm{I},0}(x,y,\omega)=\rho_\mathrm{r}H_\mathrm{r}\sum_{n=1}^{m_\mathrm{r}}\frac{\lambda_n^2\Big[I_{0,n}^-(\omega)\,X_n^-(x,\omega)-I_{0,n}^+(\omega)\,X_n^+(x,\omega)\Big]}{\beta_n(\omega)\,\kappa_n(\omega)\,\sinh[b_\mathrm{r}\kappa_n(\omega)]\cosh[b_\mathrm{r}\kappa_n(\omega)]}\,\cos[\lambda_n(\omega)\,y]\tag{18}$$

in which m_r is the number of impulsive pressure modes included in the analysis, and the parameters λ_n, $\beta_n(\omega)$, $\kappa_n(\omega)$, $X_n^-(x,\omega)$, $X_n^+(x,\omega)$, $I_{0,n}^-(\omega)$ and $I_{0,n}^+(\omega)$ are given in Appendix A. We also show in Appendix A that FRFs $\bar{p}_{\mathrm{I},j}$, $j=1\dots m_\mathrm{s}$, can be written as

$$\bar{p}_{\mathrm{I},j}(x,y,\omega)=\rho_\mathrm{r}H_\mathrm{r}\sum_{n=1}^{m_\mathrm{r}}\frac{\lambda_n^2\Big[I_{j\,n}^-(\omega)\,X_n^-(x,\omega)-I_{j\,n}^+(\omega)\,X_n^+(x,\omega)\Big]}{\beta_n(\omega)\,\kappa_n(\omega)\,\sinh[b_\mathrm{r}\kappa_n(\omega)]\cosh[b_\mathrm{r}\kappa_n(\omega)]}\,\cos[\lambda_n(\omega)\,y]\tag{19}$$

where $I_{j,n}^+(\omega)$ and $I_{j,n}^-(\omega)$ are given in Appendix A.

2.3 Convective hydrodynamic pressure

In this work, we consider rectangular water-containing structures that can be geometrically or materially asymmetric, i.e. with different lateral walls. As a consequence, the horizontal accelerations at wall-water interfaces on each side of the reservoir can be different and thus generate both symmetric and asymmetric hydrodynamic pressure waves. To account for this behavior, the FRF for convective hydrodynamic pressure $\bar{p}_\mathrm{C}$ will be decomposed into a symmetric term $\hat{\bar{p}}_\mathrm{C}$ and an antisymmetric term $\tilde{\bar{p}}_\mathrm{C}$, which correspond to symmetric and antisymmetric modes of sloshing, respectively. FRFs $\bar{p}_{\mathrm{C},0}$, and

$\bar{p}_{\mathrm{C},j}$, $j = 1 \ldots m_{\mathrm{s}}$, can then be expressed as

$$\bar{p}_{\mathrm{C},0}(x,y,\omega) = \hat{\bar{p}}_{\mathrm{C},0}(x,y,\omega) + \tilde{\bar{p}}_{\mathrm{C},0}(x,y,\omega) \tag{20}$$

$$\bar{p}_{\mathrm{C},j}(x,y,\omega) = \hat{\bar{p}}_{\mathrm{C},j}(x,y,\omega) + \tilde{\bar{p}}_{\mathrm{C},j}(x,y,\omega) \tag{21}$$

FRFs $\bar{p}_{\mathrm{C},0}$ and $\bar{p}_{\mathrm{C},j}$ are solutions of Eq. (2), and satisfy the boundary conditions described in Section 2.1, among which Eqs. (13) and (14) which relate the FRFs for convective hydrodynamic pressure to those for impulsive hydrodynamic pressure determined in Section 2.2. Accordingly, FRFs for convective hydrodynamic pressure are developed in Appendix B using the decompositions in Eqs. (20) and (21).

Considering a unit horizontal ground acceleration $\bar{\ddot{u}}_{\mathrm{g}}(\omega) = 1$, we show in Appendix B that FRF $\bar{p}_{\mathrm{C},0}$ and $\bar{p}_{\mathrm{C},j}$ can be obtained as

$$\begin{aligned} \bar{p}_{\mathrm{C},\ell}(x,y,\omega) = \sum_{m=1}^{m_{\mathrm{c}}} \sum_{n=1}^{m_{\mathrm{r}}} \Big\{ & \widehat{\Lambda}_{\ell,n,m}(\omega)\, \cosh[\hat{\kappa}_m(\omega)\, y]\, \cos[\hat{\lambda}_m(\omega)\, x] \\ & + \widetilde{\Lambda}_{\ell,n,m}(\omega)\, \cosh[\tilde{\kappa}_m(\omega)\, y]\, \sin[\tilde{\lambda}_m(\omega)\, x] \Big\}; \qquad \ell = 0, j \end{aligned} \tag{22}$$

where m_{c} is the number of reservoir convective modes and

$$\widehat{\Lambda}_{\ell,n,m}(\omega) = \frac{2 \times (-1)^{m+n}\, \rho_{\mathrm{r}} g H_{\mathrm{r}}\, \lambda_n^3(\omega) \Big[I_{\ell,n}^{+}(\omega) - I_{\ell,n}^{-}(\omega) \Big]}{b_{\mathrm{r}}\, \beta_n(\omega)\, \hat{\chi}_m(\omega) \Big[\kappa_n^2(\omega) + \hat{\lambda}_m^2(\omega) \Big] \Big[\hat{\gamma}_m^2(\omega) - \omega^2 \Big] \cosh[\hat{\kappa}_m(\omega)\, H_{\mathrm{r}}]}; \qquad \ell = 0, j \tag{23}$$

$$\widetilde{\Lambda}_{\ell,n,m}(\omega) = \frac{-2 \times (-1)^{m+n}\, \rho_{\mathrm{r}} g H_{\mathrm{r}}\, \lambda_n^3(\omega) \Big[I_{\ell,n}^{+}(\omega) + I_{\ell,n}^{-}(\omega) \Big]}{b_{\mathrm{r}}\, \beta_n(\omega)\, \tilde{\chi}_m(\omega) \Big[\kappa_n^2(\omega) + \tilde{\lambda}_m^2(\omega) \Big] \Big[\tilde{\gamma}_m^2(\omega) - \omega^2 \Big] \cosh[\tilde{\kappa}_m(\omega)\, H_{\mathrm{r}}]}; \qquad \ell = 0, j \tag{24}$$

in which the frequency-dependent functions $\hat{\gamma}_m^2$ and $\tilde{\gamma}_m^2$ are given for $m = 1 \ldots m_{\mathrm{c}}$ by

$$\hat{\gamma}_m^2(\omega) = \frac{g\, \hat{\kappa}_m(\omega)}{\hat{\chi}_m(\omega)} \tanh[\hat{\kappa}_m(\omega)\, H_{\mathrm{r}}]; \qquad \tilde{\gamma}_m^2(\omega) = \frac{g\, \tilde{\kappa}_m(\omega)}{\tilde{\chi}_m(\omega)} \tanh[\tilde{\kappa}_m(\omega)\, H_{\mathrm{r}}] \tag{25}$$

where the parameters $\hat{\chi}_m$, $\tilde{\chi}_m$, $\hat{\kappa}_m$ and $\tilde{\kappa}_m$ are obtained as

$$\hat{\chi}_m(\omega) = 1 + \frac{\rho_{\mathrm{i}} h_{\mathrm{i}}}{\rho_{\mathrm{r}}}\, \hat{\kappa}_m(\omega)\, \tanh[\hat{\kappa}_m(\omega)\, H_{\mathrm{r}}]; \qquad \tilde{\chi}_m(\omega) = 1 + \frac{\rho_{\mathrm{i}} h_{\mathrm{i}}}{\rho_{\mathrm{r}}}\, \tilde{\kappa}_m(\omega)\, \tanh[\tilde{\kappa}_m(\omega)\, H_{\mathrm{r}}] \tag{26}$$

$$\hat{\kappa}_m(\omega) = \sqrt{\hat{\lambda}_m^2 - \frac{\omega^2}{C_{\mathrm{r}}^2}}; \qquad \tilde{\kappa}_m(\omega) = \sqrt{\tilde{\lambda}_m^2 - \frac{\omega^2}{C_{\mathrm{r}}^2}} \tag{27}$$

in which the eigenvalues $\hat{\lambda}_m$ and $\tilde{\lambda}_m$ corresponding to convective symmetric and antisymmetric modes, respectively, are given for $m = 1 \ldots m_{\mathrm{c}}$ by

$$\hat{\lambda}_m = \frac{m\, \pi}{b_{\mathrm{r}}}; \qquad \tilde{\lambda}_m = \frac{(2\, m - 1)\, \pi}{2\, b_{\mathrm{r}}} \tag{28}$$

The natural convective symmetric and antisymmetric frequencies correspond to the frequencies $\hat{\omega}_m$ and $\tilde{\omega}_m$, respectively, that satisfy the equations

$$\hat{\gamma}_m^2(\hat{\omega}_m) - \hat{\omega}_m^2 = 0\,; \qquad \tilde{\gamma}_m^2(\tilde{\omega}_m) - \tilde{\omega}_m^2 = 0 \tag{29}$$

for $m = 1 \ldots m_{\mathrm{c}}$. If water is assumed incompressible, then the parameters $\hat{\kappa}_m$ and $\tilde{\kappa}_m$ become frequency-independent, and Eq. (27) simplifies to

$$\hat{\kappa}_m = \hat{\lambda}_m\,; \qquad \tilde{\kappa}_m = \tilde{\lambda}_m \tag{30}$$

The natural convective symmetric and antisymmetric frequencies $\hat{\omega}_m$ and $\tilde{\omega}_m$, respectively, become also frequency-independent, and can be obtained for $m = 1 \ldots m_{\mathrm{c}}$ as

$$\hat{\omega}_m = \sqrt{\frac{g\,\hat{\kappa}_m}{\hat{\chi}_m}\tanh(\hat{\kappa}_m\,H_{\mathrm{r}})}; \qquad \tilde{\omega}_m = \sqrt{\frac{g\,\tilde{\kappa}_m}{\tilde{\chi}_m}\tanh(\tilde{\kappa}_m\,H_{\mathrm{r}})} \tag{31}$$

2.4 Time responses for a seismic loading

The generalized coordinate vector $\bar{\mathbf{Z}}$ is computed after substituting the impulsive and convective FRFs into Eq. (15), then the total pressure in the frequency-domain is computed according to Eq. (6). The time-history displacements and accelerations of a point of the lateral walls subjected to a ground acceleration $\ddot{u}_{\mathrm{g}}(t)$ can be obtained as

$$u(x,y,t) = \sum_{j=1}^{N_{\mathrm{s}}} \psi_j^{(x)}(x,y)\,Z_j(t)\,; \qquad \ddot{u}(x,y,t) = \sum_{j=1}^{m_{\mathrm{s}}} \psi_j^{(x)}(x,y)\,\ddot{Z}_j(t) \tag{32}$$

$$v(x,y,t) = \sum_{j=1}^{N_{\mathrm{s}}} \psi_j^{(y)}(x,y)\,Z_j(t)\,; \qquad \ddot{v}(x,y,t) = \sum_{j=1}^{m_{\mathrm{s}}} \psi_j^{(y)}(x,y)\,\ddot{Z}_j(t) \tag{33}$$

where the time-domain generalized coordinates Z_j are given by the Fourier integrals

$$Z_j(t) = \frac{1}{2\pi}\int_{-\infty}^{\infty} \bar{Z}_j(\omega)\,\bar{\ddot{u}}_{\mathrm{g}}(\omega)\,\mathrm{e}^{\mathrm{i}\omega t}\,\mathrm{d}\omega\,; \qquad \ddot{Z}_j(t) = -\frac{1}{2\pi}\int_{-\infty}^{\infty} \omega^2 \bar{Z}_j(\omega)\,\bar{\ddot{u}}_{\mathrm{g}}(\omega)\,\mathrm{e}^{\mathrm{i}\omega t}\,\mathrm{d}\omega \tag{34}$$

in which $\bar{\ddot{u}}_{\mathrm{g}}(\omega)$ is the Fourier transform of the ground acceleration $\ddot{u}_{\mathrm{g}}(t)$

$$\bar{\ddot{u}}_{\mathrm{g}}(\omega) = \int_0^{t_a} u_{\mathrm{g}}(t)\,\mathrm{e}^{-\mathrm{i}\omega t}\,\mathrm{d}t \tag{35}$$

with t_a denoting the time duration of the applied accelerogram.

The time-history response for total hydrodynamic pressure p and vertical displacement ζ at reservoir surface under the effect of ground acceleration $\ddot{u}_{\mathrm{g}}(t)$ can also be obtained as

$$p(x,y,t) = p_0(x,y,t) + \sum_{j=1}^{m_{\mathrm{s}}} p_j(x,y,t)\,\ddot{Z}_j(t) \tag{36}$$

$$\zeta(x,t)=\frac{1}{\rho_{\mathrm{r}}g}\,p(x,H_{\mathrm{r}},t) \tag{37}$$

Based on the above relations, other quantities of interest such as shear forces or overturning moments, can also be determined.

In the coupled systems studied, two types of damping should be accounted for to model the dissipation of energy in the solid containing structure and in the contained fluid. A viscous damping has to be applied to represent energy dissipation in the vibrating structure and associated impulsive modes. A damping for convective modes is introduced to mainly account for energy dissipation within the contained fluid, and is generally assumed to be less than 0.5% for light viscosity liquids without dissipative devices. Various design codes like the Eurocode 8 (2003) or the ACI 350.3 (2006) specify 0.5% damping for convective modes and 5% damping for impulsive modes. These conservative values are based on several studies such as (Scarsi, 1971; Martel et al., 1998; Ghaemmaghami and Kianoush, 2010). They are used in the numerical models presented next.

In the analytical formulation, damping for impulsive modes is represented by a hysteretic damping factor η_{s} included in Eq. (16). Damping for convective modes is accounted for through a viscous damping ξ_{c} introduced into Eqs. (38) and (39) to yield

$$\widehat{\Lambda}_{\ell,n,m}(\omega)=\frac{2\times(-1)^{m+n}\,\rho_{\mathrm{r}}gH_{\mathrm{r}}\,\lambda_n^3(\omega)\Big[I^{+}_{\ell,n}(\omega)-I^{-}_{\ell,n}(\omega)\Big]}{b_{\mathrm{r}}\,\beta_n(\omega)\,\hat{\chi}_m(\omega)\,\Big[\kappa_n^2(\omega)+\hat{\lambda}_m^2(\omega)\Big]\,\Big[\hat{\gamma}_m^2(\omega)+2\,\mathrm{i}\,\xi_{\mathrm{c}}\,\omega\,\hat{\gamma}_m(\omega)-\omega^2\Big]\,\cosh[\hat{\kappa}_m(\omega)\,H_{\mathrm{r}}]} \tag{38}$$

$$\widetilde{\Lambda}_{\ell,n,m}(\omega)=\frac{-2\times(-1)^{m+n}\,\rho_{\mathrm{r}}gH_{\mathrm{r}}\,\lambda_n^3(\omega)\Big[I^{+}_{\ell,n}(\omega)+I^{-}_{\ell,n}(\omega)\Big]}{b_{\mathrm{r}}\,\beta_n(\omega)\,\tilde{\chi}_m(\omega)\,\Big[\kappa_n^2(\omega)+\tilde{\lambda}_m^2(\omega)\Big]\,\Big[\tilde{\gamma}_m^2(\omega)+2\,\mathrm{i}\,\xi_{\mathrm{c}}\,\omega\,\tilde{\gamma}_m(\omega)-\omega^2\Big]\,\cosh[\tilde{\kappa}_m(\omega)\,H_{\mathrm{r}}]} \tag{39}$$

for $\ell=0,j$.

The proposed method is validated in the next section through a numerical example illustrating the dynamic response symmetric and asymmetric water-containing structures covered with floating ice blocks.

3 Illustrative numerical example

3.1 Properties of the studied system and numerical modeling

We consider the geometrically asymmetric wall-water system illustrated in Fig. 3. It consists of two lateral walls impounding a reservoir of height $H_{\mathrm{r}}=20$ m and a length $L_{\mathrm{r}}=20$ m, covered with floating ice blocks. The following properties are adopted for the constitutive material of the walls: modulus of elasticity $E_{\mathrm{s}}=25$ GPa, Poisson's ratio $\nu_{\mathrm{s}}=0.2$, and mass density $\rho_{\mathrm{s}}=2400$ kg/m^3. The water is assumed compressible, with a velocity of pressure waves $C_{\mathrm{r}}=1440$ m/s, and a mass density $\rho_{\mathrm{r}}=1000$ kg/m^3. An ice mass density $\rho_{\mathrm{i}}=917$ kg/m^3 is adopted (USACE, 2002). Although the thickness of the ice blocks may vary from one point to another, an average uniform thickness $h_\mathrm{i} = 1.0\,$m is considered for this numerical example.

The application of the proposed method first requires the determination of the mode shapes ψ_j, $j = 1 \ldots m_\mathrm{s}$, of the lateral walls without water, i.e. dry structure. For this purpose, both walls are discretized into 4-node plane-strain solid finite elements using the software ADINA (2010) as illustrated in Fig. 4 (a). Fig. 5 shows the obtained first four mode shapes, i.e. $m_\mathrm{s} = 4$, given by ADINA (2010) as well as the corresponding frequencies and horizontal effective modal masses expressed in percentage of total mass of the walls. Convergence studies showed that $m_\mathrm{c} = 30$ convective modes are required. A viscous damping ratio $\xi_\mathrm{c} = 0.5\%$ and a hysteretic damping factor $\eta_\mathrm{s} = 0.1$ are applied to damp-out convective and impulsive modes, respectively.

To validate the proposed formulation, we build a coupled fluid-structure finite element model where both the walls and the reservoir are modeled using 4-node plane strain and 4-node potential-based finite elements programmed in ADINA (2010), respectively. Fig. 4 (b) illustrates the finite element mesh used. In this case, a potential-based formulation of the fluid domain is adopted (Everstine, 1981; Bouaanani and Lu, 2009). Dynamic interaction between the walls and the reservoir is achieved through fluid-structure interface elements. Beam elements with negligible stiffness are introduced at the reservoir surface to account for fluid-structure interaction between the reservoir and the floating ice blocks. Two modal viscous damping values are assumed to damp-out convective and impulsive modes, respectively: (i) a 0.5% modal damping ratio is applied to the first 30 modes with low frequencies corresponding to convective modes only, and (ii) a 5% modal damping ratio is applied to the rest of the modes up to the $210\,$th.

The frequency- and time-domain dynamic responses of the wall-water system are investigated next using the previously described analytical and finite element models shown in Figs. 4 (a) and (b).

3.2 Frequency-domain response

Fig. 6 presents the FRFs for nondimensionalized hydrodynamic pressures $|\bar{p}/(\rho_\mathrm{r} g H_\mathrm{r})|$ obtained at points A and A', nondimensionalized horizontal relative displacements $|\bar{u}/u_\mathrm{st}|$ at points C and C', where u_st is the lateral static displacement under the effect of hydrostatic pressure, and nondimensionalized vertical displacement ζ/H_r at points B and B' at reservoir surface. The results are determined at points A, B and C located on the left wall, and points A', B' and C' belonging to the right wall as indicated in Fig. 4. The vertical positions of the points are $y_\mathrm{A} = y_\mathrm{A'} = 1\,$m, $y_\mathrm{B} = y_\mathrm{B'} = 20\,$m, $y_\mathrm{C} = 24\,$m and $y_\mathrm{C'} = 28\,$m. The FRFs in Fig. 6 clearly show that the proposed formulation yields excellent results when compared to those obtained through finite element modeling whether with or without the presence of floating ice blocks. Each frequency curve exhibits: (i) a lower frequency range part, i.e. $f \leqslant 0.5\,$Hz, corresponding to convective modes, and (ii) a higher frequency range part, i.e. $f \geqslant 1.5\,$Hz, corresponding to impulsive modes. The FRFs of hydrodynamic pressures at reservoir's bottom and the lateral displacements at the top of the walls show that the presence of floating ice blocks affects dynamic responses corresponding to convective modes and to a much larger extent those corresponding to the impulsive ones. As can be seen, the main effect is a decrease of resonant frequencies, a behavior that can be related to the added mass from floating ice blocks. We also observe that the FRFs of vertical displacements at reservoir surface are the most affected by the presence of ice blocks, which mainly leads to the appearance of impulsive modes with resonant frequencies larger than 1.5 Hz.

The techniques described previously are applied next to determine convective and impulsive hydrodynamic pressure profiles corresponding to frequencies $0.9\,\tilde{\omega}_1$, $1.1\,\tilde{\omega}_1$, $0.9\,\bar{\omega}_1$ and $1.1\,\bar{\omega}_1$, where $\tilde{\omega}_1$ and $\bar{\omega}_1$ denote the natural frequencies corresponding to the first antisymmetric convective mode and first impulsive mode, respectively. The resulting hydrodynamic profiles illustrated in Fig. 7 confirm that the proposed formulation is in excellent agreement with the advanced finite element solution. The profiles also reveal that the presence of ice blocks: (i) slightly decreases the amplitude of convective hydrodynamic pressure along the height of the reservoir, and (ii) increases the amplitude of impulsive hydrodynamic pressure, with maximum amplification observed at reservoir surface.

3.3 Time-domain response

In this section, we investigate the performance of the proposed method in assessing the seismic response of the previously described wall-water system. The horizontal acceleration component of Imperial Valley earthquake (1940) at El Centro is selected to conduct the analyses using the proposed and finite element techniques described above. Fig. 8 illustrates the first 20 s of the input ground acceleration. The obtained time-histories of nondimensionalized horizontal relative displacements $|u/u_{\mathrm{st}}|$ at points C and C', the nondimensionalized shear forces V/F_{stat} at sections A and A', where $F_{\mathrm{stat}} = \rho_{\mathrm{r}} g H_{\mathrm{r}}^2/2$ denotes the hydrostatic force, and the vertical displacements ζ at points B and B' at reservoir surface are shown in Figs. 9 and 10 for the reservoir with free surface and ice-covered, respectively. These figures show that the time-history results given by the developed formulation and the finite element solution are practically coincident.

We observe that the amplitudes of all the quantities studied increase with the presence of floating ice blocks. This effect is maximum for the vertical displacements ζ at reservoir surface, with displacements approximately 5 times larger with an ice-covered reservoir than with a free surface case. We also note that the frequency content of the response curves is affected by the presence of ice blocks. This is more pronounced in the response curves of reservoir surface vertical displacements as we compare Figs. 9 (e) and (f) to Figs. 10 (e) and (f). Low convective frequencies dominate indeed the free surface reservoir dynamic response as anticipated from the FRF of reservoir surface vertical displacement shown in Fig. 6 (e), which explains the predominant long period oscillations in the time-domaine response of free surface vertical displacements in Figs. 9 (e) and (f). We also note the obvious opposition of phase of vertical displacements at points B and B', which originates from predominant first antisymmetric sloshing mode. On the other hand, Fig. 6 (f) shows that the FRF of vertical displacement of ice-covered reservoir surface also contains low frequency convective modes, but more importantly impulsive modes with resonant frequencies larger than 1.5 Hz, similarly to the FRFs of hydrodynamic pressure or lateral displacements in Figs. 6 (a) to (d). These impulsive modes are predominant in the time-domain response of ice-covered reservoir surface vertical displacements shown in Figs. 9 (e) and (f), which explains the approximate resemblance of their time-history signature to that of lateral displacements and base shears in Figs. 9 (a) to (d), also dominated by impulsive modes. We see from the latter figures that maximum displacements at top of container lateral walls are amplified by about 1.5 times due to the presence of floating ice blocks, while the shear force at the base of the walls is not significantly affected.

Finally, the proposed formulation is used to illustrate the effect of asymmetry of the previous ice-covered water-containing structure on its dynamic response. For this purpose, we consider a symmetric rectangular water-containing structure made by replacing the right wall of the asymmetric structure in Fig. 3 by its 3 m-thick and 24 m-high rectangular left wall. The dimensions of the reservoir are the same as the asymmetric wall-water system. The symmetric water-containing structure is subjected to the same earthquake as previously. The time-histories of nondimensionalized horizontal displacements $|u/u_{\mathrm{st}}|$ at point C, as well as vertical displacements ζ at points B and B' at reservoir surface obtained using the developed method are illustrated in Fig. 11 for the symmetric and asymmetric water-containing structures. The results in Figs. 11 (a) and (b) show that asymmetry has a minor effect of the structural response of the walls either with or without ice blocks. The vertical displacements of reservoir surface at point B are also practically insensitive to asymmetry with or without ice blocks as observed in Figs. 11 (c) and (d). Figs. 11 (e) and (f) reveal however that the vertical displacements of reservoir surface at point B' are affected by asymmetry under free surface conditions, and to a much larger extent when the reservoir is covered by ice blocks. This result emphasizes that, for the particular water-containing structures studied, the presence of ice blocks increases the impact of asymmetry on hydrodynamic response indicators such as displacement fluctuations at reservoir surface.

4 Conclusions

This paper presented a new formulation to investigate the effects of floating ice blocks on seismically-excited rectangular water-containing structures. The proposed method is based on a sub-structuring approach, where the flexible containing structure and ice-added mass are modeled using finite elements, while hydrodynamic effects are modeled analytically through interaction forces at the water-structure and water-ice interfaces, thus eliminating the need for reservoir finite element discretization. In addition to accounting for the influence of floating ice blocks and container walls' flexibility, the developed frequency- and time-domain techniques also include the effects of container asymmetry as well as the coupling between convective and impulsive components of hydrodynamic pressure. The application of the proposed formulation is illustrated through a numerical example illustrating the dynamic response of an asymmetric water-containing structure covered with floating ice blocks, as well as that of an equivalent symmetric structure containing a reservoir with the same dimensions. The obtained time- and frequency-domain responses showed that the proposed formulation yields excellent results when compared to those from coupled fluid-structure finite element modeling either with or without the presence of floating ice blocks. For the water-containing structures studied, we observed that the presence of floating ice blocks mainly affects dynamic responses corresponding to convective and impulsive modes as follows: (i) a slight decrease of convective frequencies and a more important decrease of impulsive ones, mainly due to the added mass from the floating ice blocks; (ii) a slight decrease of the amplitude of convective hydrodynamic pressure along the height of the reservoir; (iii) an increase of the amplitude of impulsive hydrodynamic pressure, with maximum amplification observed at reservoir surface; (iv) an increase of the amplitudes of displacements, shear forces and, in particular, vertical sloshing displacements at reservoir surface.

List of symbols

Abbreviations

FRF	frequency response function

Symbols

$A_{n,0}$, $A_{n,j}$, $A'_{n,0}$ and $A'_{n,j}$	coefficients used for mathematical derivations in Appendix A
$B_{m,0}$, $B_{m,j}$, $B'_{m,0}$ and $B'_{m,j}$	coefficients used for mathematical derivations in Appendix B
a_g	amplitude of harmonic ground acceleration
$\bar{\ddot{u}}_\mathrm{g}$	Fourier transform of ground acceleration $\ddot{u}_\mathrm{g}$
b_r	half-length of the reservoir
C_r	compression wave velocity within the reservoir
ℓ	index referring to rigid body motion effects when $\ell = 0$ and to lateral vibrations along structural mode j when $\ell = j$
E_s	modulus of elasticity of the containing structure
F_stat	hydrostatic force
g	acceleration due to gravity
h_i	average thickness of the floating ice blocks
H_r	height of the reservoir

$I^{-}_{0,n}$ and $I^{+}_{0,n}$	parameters given by Eq. (A11) for $n=1\dots m_\mathrm{r}$
$I^{-}_{j,n}$ and $I^{+}_{j,n}$	parameters given by Eqs. (A12) and (A13) for $j=1\dots m_\mathrm{s}$ and $n=1\dots m_\mathrm{r}$
L_r	length of the reservoir
$\mathbf{M}$	mass matrice of the ice-container system
m_c	number of reservoir convective modes
m_r	number of impulsive pressure reservoir modes included in the analysis
m_s	number of structural mode shapes included in the analysis
p and $\bar{b}$	hydrodynamic pressure and corresponding FRF, respectively
$\bar{p}_0$	FRF for hydrodynamic pressure due to rigid body motion of the containing structure subjected to ground acceleration $\bar{\ddot{u}}_\mathrm{g}$
$\bar{p}_j$	FRF for hydrodynamic pressure due to horizontal ground accelerations $\psi_j^{(x)}(-b_\mathrm{r}, y)$ and $\psi_j^{(x)}(b_\mathrm{r}, y)$ of the lateral walls vibrating along structural mode j
$\bar{p}_\mathrm{I}$ and $\bar{p}_\mathrm{C}$	impulsive and convective components of hydrodynamic pressure FRF $\bar{b}$
$\bar{p}_{\mathrm{I},0}$ and $\bar{p}_{\mathrm{C},0}$	impulsive and convective components of hydrodynamic pressure FRF $\bar{b}_0$
$\bar{p}_{\mathrm{I},j}$ and $\bar{p}_{\mathrm{C},j}$	impulsive and convective components of hydrodynamic pressure FRF $\bar{b}_j$
$\hat{\bar{p}}_\mathrm{C}$ and $\tilde{\bar{p}}_\mathrm{C}$	symmetric and antisymmetric components of convective hydrodynamic pressure FRF $\bar{p}_\mathrm{C}$, respectively
$\hat{\bar{p}}_{\mathrm{C},0}$ and $\tilde{\bar{p}}_{\mathrm{C},0}$	symmetric and antisymmetric components of convective hydrodynamic pressure FRF $\bar{p}_{\mathrm{C},0}$, respectively
$\hat{\bar{p}}_{\mathrm{C},j}$ and $\tilde{\bar{p}}_{\mathrm{C},j}$	symmetric and antisymmetric components of convective hydrodynamic pressure FRF $\bar{p}_{\mathrm{C},j}$, respectively
$\bar{\mathbf{Q}}$ and $\bar{Q}_n$	vector in Eq. (15) and its elements given by Eq. (17) for $n=1\dots m_\mathrm{s}$, respectively
$\bar{\mathbf{S}}$ and $\bar{S}_{nj}$	matrix in Eq. (15) and its elements given by Eq. (16) for $n=1\dots m_\mathrm{s}$ and $j=1\dots m_\mathrm{s}$, respectively
t	time variable
t_a	time duration of the applied accelerogram

x and y	horizontal and vertical axes of Cartesian coordinate system, respectively
X_n^- and X_n^+	parameters given by Eq. (A14) for $n = 1 \ldots m_\mathrm{r}$
u and v	time-history response of horizontal and vertical structural displacements, respectively
u_st	lateral static displacement under the effect of hydrostatic pressure
$\bar{u}$ and $\bar{v}$	FRFs of horizontal and vertical structural displacements, respectively
$\ddot{u}_\mathrm{g}$	time-history of ground acceleration
$\bar{\ddot{u}}$ and $\bar{\ddot{v}}$	FRFs of horizontal and the vertical structural accelerations, respectively
V	shear force
$\bar{\mathbf{Z}}$ and $\bar{Z}_j$	vector of generalized coordinates and j th generalized coordinate, respectively
$\mathbf{1}$	column-vector with the same dimension as the vector of nodal relative displacements, containing zeros except along horizontal degrees of freedom which correspond to the direction of earthquake excitation
β_n	parameter given by Eq. (A10) for $n = 1 \ldots m_\mathrm{r}$
$\hat{\gamma}_m$ and $\tilde{\gamma}_m$	parameters given by Eq. (25) for $m = 1 \ldots m_\mathrm{c}$
δ	Kronecker symbol
ζ	vertical displacement at reservoir surface
η_s	structural hysteretic damping factor
κ_n	parameter given by Eq. (A3) for $n = 1 \ldots m_\mathrm{r}$
$\hat{\kappa}_m$ and $\tilde{\kappa}_m$	parameters given by Eq. (27) for $m = 1 \ldots m_\mathrm{c}$
λ_n	eigenvalue given by Eq. (A3) for $n = 1 \ldots m_\mathrm{r}$
$\hat{\lambda}_m$ and $\tilde{\lambda}_m$	eigenvalues given by Eq. (28) for $m = 1 \ldots m_\mathrm{c}$
$\widehat{\Lambda}_{\ell,n,m}$ and $\widetilde{\Lambda}_{\ell,n,m}$	parameters given by Eqs. (38) and (39), respectively, for $\ell = 0, j$, $m = 1 \ldots m_\mathrm{c}$ and $n = 1 \ldots m_\mathrm{r}$
∇^2	Laplace differential operator
ν_s	Poisson's ratio of the containing structure

ξ_c	viscous damping associated with convective modes
ρ_i	mass density of floating ice blocks
ρ_r	mass density of water
ρ_s	mass density of the containing structure
$\boldsymbol{\psi}_n$	n th mode shape of the empty containing structure combined to ice-added mass
$\hat{\chi}_m$ and $\tilde{\chi}_m$	parameters given by Eq. (26) for $m=1\ldots m_\mathrm{c}$
$\psi_j^{(x)}$ and $\psi_j^{(y)}$	x- and y-components of the j th structural mode shape, respectively
ω	exciting frequency
ω_n	vibration frequency corresponding to structural mode shape $\boldsymbol{\psi}_n$ of the empty containing structure combined to ice-added mass
$\bar{\omega}_m$	m th impulsive frequency
$\hat{\omega}_m$ and $\tilde{\omega}_m$	m th convective symmetric and antisymmetric frequencies, respectively

Acknowledgements

The authors would like to acknowledge the financial support of the Natural Sciences and Engineering Research Council of Canada (NSERC) and the Quebec Research Funds for Natural Sciences and Engineering (FRQNT).

APPENDIX A

Using Eqs.(2), (12) and the boundary conditions in the left column of Eqs. (9) and (10), we show that FRFs $\bar{p}_{\mathrm{I},0}$ and $\bar{p}_{\mathrm{I},j}$, $j = 1 \ldots m_{\mathrm{s}}$, can be expressed as

$$\bar{p}_{\mathrm{I},0}(x, y, \omega) = \sum_{n=1}^{m_{\mathrm{r}}} \left[A_{n,0}(\omega)\, \mathrm{e}^{-\kappa_n(\omega)\, x} + A'_{n,0}(\omega)\, \mathrm{e}^{\kappa_n(\omega)\, x} \right] \cos(\lambda_n\, y) \tag{A1}$$

$$\bar{p}_{\mathrm{I},j}(x, y, \omega) = \sum_{n=1}^{m_{\mathrm{r}}} \left[A_{n,j}(\omega)\, \mathrm{e}^{-\kappa_n(\omega)\, x} + A'_{n,j}(\omega)\, \mathrm{e}^{\kappa_n(\omega)\, x} \right] \cos(\lambda_n\, y) \tag{A2}$$

where m_{r} is the number of impulsive pressure modes and frequency-dependent coefficients $A_{n,0}$, $A_{n,j}$, $A'_{n,0}$ and $A'_{n,j}$ are to be determined later, and eigenvalues λ_n and frequency-dependent parameters κ_n are given for $n = 1 \ldots m_{\mathrm{r}}$ by

$$\lambda_n = \frac{(2\, n - 1)\, \pi}{2 H_{\mathrm{r}}}\, ; \qquad\qquad \kappa_n = \sqrt{\lambda_n^2 - \frac{\omega^2}{C_{\mathrm{r}}^2}} \tag{A3}$$

Substitution of Eqs. (A1) and (A2) into the boundary conditions in the left column of Eqs. (7) and (8) yields

$$\sum_{n=1}^{m_{\mathrm{r}}} \kappa_n(\omega) \left[- A_{n,0}(\omega)\, \mathrm{e}^{-\kappa_n(\omega)\, b_{\mathrm{r}}} + A'_{n,0}(\omega)\, \mathrm{e}^{\kappa_n(\omega)\, b_{\mathrm{r}}} \right] \cos(\lambda_n\, y) = -\rho_{\mathrm{r}} \tag{A4}$$

$$\sum_{n=1}^{m_{\mathrm{r}}} \kappa_n(\omega) \left[- A_{n,0}(\omega)\, \mathrm{e}^{\kappa_n(\omega)\, b_{\mathrm{r}}} + A'_{n,0}(\omega)\, \mathrm{e}^{-\kappa_n(\omega)\, b_{\mathrm{r}}} \right] \cos(\lambda_n\, y) = -\rho_{\mathrm{r}} \tag{A5}$$

$$\sum_{n=1}^{m_{\mathrm{r}}} \kappa_n(\omega) \left[- A_{n,j}(\omega)\, \mathrm{e}^{-\kappa_n(\omega)\, b_{\mathrm{r}}} + A'_{n,j}(\omega)\, \mathrm{e}^{\kappa_n(\omega)\, b_{\mathrm{r}}} \right] \cos(\lambda_n\, y) = -\rho_{\mathrm{r}}\, \psi_j^{(x)}(b_{\mathrm{r}}, y) \tag{A6}$$

$$\sum_{n=1}^{m_{\mathrm{r}}} \kappa_n(\omega) \left[- A_{n,j}(\omega)\, \mathrm{e}^{\kappa_n(\omega)\, b_{\mathrm{r}}} + A'_{n,j}(\omega)\, \mathrm{e}^{-\kappa_n(\omega)\, b_{\mathrm{r}}} \right] \cos(\lambda_n\, y) = -\rho_{\mathrm{r}}\, \psi_j^{(x)}(-b_{\mathrm{r}}, y) \tag{A7}$$

Multiplying Eqs. (A4) to (A7) by $\cos(\lambda_n\, y)$, integrating over reservoir height and using the orthogonality properties of trigonometric functions yields to a system of $4 m_{\mathrm{r}}$ linear equations which can be solved for coefficients $A_{n,0}$, $A'_{n,0}$, $A_{n,j}$ and $A'_{n,j}$, $n = 1 \ldots m_{\mathrm{r}}$, $j = 1 \ldots m_{\mathrm{s}}$, as follows

$$A_{n,\ell}(\omega) = \frac{\rho_{\mathrm{r}} H_{\mathrm{r}} \lambda_n^2 \left[I^-_{\ell,n}(\omega)\, \mathrm{e}^{b_{\mathrm{r}} \kappa_n(\omega)} - I^+_{\ell,n}(\omega)\, \mathrm{e}^{-b_{\mathrm{r}} \kappa_n(\omega)} \right]}{2 \beta_n(\omega)\, \kappa_n(\omega)\, \sinh[b_{\mathrm{r}} \kappa_n(\omega)] \cosh[b_{\mathrm{r}} \kappa_n(\omega)]}\, ; \qquad \ell = 0, j \tag{A8}$$

$$A'_{n,\ell}(\omega) = \frac{\rho_{\mathrm{r}} H_{\mathrm{r}} \lambda_n^2 \left[I^-_{\ell,n}(\omega)\, \mathrm{e}^{-b_{\mathrm{r}} \kappa_n(\omega)} - I^+_{\ell,n}(\omega)\, \mathrm{e}^{b_{\mathrm{r}} \kappa_n(\omega)} \right]}{2 \beta_n(\omega)\, \kappa_n(\omega)\, \sinh[b_{\mathrm{r}} \kappa_n(\omega)] \cosh[b_{\mathrm{r}} \kappa_n(\omega)]}\, ; \qquad \ell = 0, j \tag{A9}$$

in which

$$\beta_n = H_{\mathrm{r}}\, \lambda_n^2 \tag{A10}$$

and $I^{-}_{0,n}$, $I^{+}_{0,n}$, $I^{-}_{j,n}$ and $I^{+}_{j,n}$ are given by

$$I^{-}_{0,n}(\omega) \;=\; I^{+}_{0,n}(\omega) = \frac{1}{H_\mathrm{r}} \int_0^{H_\mathrm{r}} \cos(\lambda_n\, y)\,\mathrm{d}y = \frac{2 \times (-1)^{n+1}\, H_\mathrm{r}}{2n-1} \tag{A11}$$

$$I^{-}_{j,n}(\omega) \;=\; \frac{1}{H_\mathrm{r}} \int_0^{H_\mathrm{r}} \psi_j^{(x)}(-b_\mathrm{r}, y)\; \cos(\lambda_n\, y)\,\mathrm{d}y \tag{A12}$$

$$I^{+}_{j,n}(\omega) \;=\; \frac{1}{H_\mathrm{r}} \int_0^{H_\mathrm{r}} \psi_j^{(x)}(b_\mathrm{r}, y)\; \cos(\lambda_n\, y)\,\mathrm{d}y \tag{A13}$$

Substituting Eqs. (A8) and (A9) into Eqs. (A1) and (A2) yields the expressions of $\bar{p}_{\mathrm{I},0}$ and $\bar{p}_{\mathrm{I},j}$ given in Eqs. (18) and (19), respectively, with the coefficients X^{-}_{n} and X^{+}_{n} obtained as

$$X^{-}_{n}(x,\omega) = \cosh\big[(x-b_\mathrm{r})\,\kappa_n(\omega)\big]\,; \qquad\qquad X^{+}_{n}(x,\omega) = \cosh\big[(x+b_\mathrm{r})\,\kappa_n(\omega)\big] \tag{A14}$$

APPENDIX B

Using Eqs. (2), and the boundary conditions in the right column of Eqs. (7), (8), (9) and (10), we show that FRFs $\bar{p}_{\mathrm{C},0}$ and $\bar{p}_{\mathrm{C},j}$, $j=1\ldots m_{\mathrm{s}}$, can be expressed as

$$\bar{p}_{\mathrm{C},0}(x,y,\omega) = \sum_{m=1}^{m_{\mathrm{c}}} \Big\{ B_{m,0}(\omega)\,\cosh\left[\hat{\kappa}_m(\omega)\,y\right]\,\cos(\hat{\lambda}_m\,x) + B'_{m,0}(\omega)\,\cosh\left[\tilde{\kappa}_m(\omega)\,y\right]\,\sin(\tilde{\lambda}_m\,x)\Big\} \quad \text{(B1)}$$

$$\bar{p}_{\mathrm{C},j}(x,y,\omega) = \sum_{m=1}^{m_{\mathrm{c}}} \Big\{ B_{m,j}(\omega)\,\cosh\left[\hat{\kappa}_m(\omega)\,y\right]\,\cos(\hat{\lambda}_m\,x) + B'_{m,j}(\omega)\,\cosh\left[\tilde{\kappa}_m(\omega)\,y\right]\,\sin(\tilde{\lambda}_m\,x)\Big\} \quad \text{(B2)}$$

where m_{c} is the number of reservoir convective modes and frequency-dependent coefficients $B_{m,0}$, $B_{m,j}$, $B'_{m,0}$ and $B'_{m,j}$ are to be determined later, and eigenvalues $\hat{\lambda}_m$ and $\tilde{\lambda}_m$, and frequency-dependent parameters $\hat{\kappa}_m$ and $\tilde{\kappa}_m$ are given for $m=1\ldots m_{\mathrm{c}}$ by

$$\hat{\lambda}_m = \frac{m\pi}{b_{\mathrm{r}}}\,; \qquad \hat{\kappa}_m(\omega) = \sqrt{\hat{\lambda}_m^2 - \frac{\omega^2}{C_{\mathrm{r}}^2}} \quad \text{(B3)}$$

$$\tilde{\lambda}_m = \frac{(2m-1)\,\pi}{2b_{\mathrm{r}}}\,; \qquad \tilde{\kappa}_m(\omega) = \sqrt{\tilde{\lambda}_m^2 - \frac{\omega^2}{C_{\mathrm{r}}^2}} \quad \text{(B4)}$$

Substitution of Eqs. (B1) and (B2) into the boundary conditions in Eqs. (13) and (14) yields

$$\begin{aligned}\sum_{m=1}^{m_{\mathrm{c}}} \Big\{ & B_{m,0}(\omega)\,\hat{\chi}_m(\omega)\,\cosh\left[\hat{\kappa}_m(\omega)\,H_{\mathrm{r}}\right]\,\cos(\hat{\lambda}_m\,x)\left[\hat{\gamma}_m^2(\omega)-\omega^2\right] \\ & + B'_{m,0}(\omega)\,\tilde{\chi}_m(\omega)\,\cosh\left[\tilde{\kappa}_m(\omega)\,H_{\mathrm{r}}\right]\,\sin(\tilde{\lambda}_m\,x)\left[\tilde{\gamma}_m^2(\omega)-\omega^2\right]\Big\} = -g\,\frac{\partial\bar{p}_{\mathrm{I},0}}{\partial y}(x,H_{\mathrm{r}},\omega)\end{aligned} \quad \text{(B5)}$$

$$\begin{aligned}\sum_{m=1}^{m_{\mathrm{c}}} \Big\{ & B_{m,j}(\omega)\,\hat{\chi}_m(\omega)\,\cosh\left[\hat{\kappa}_m(\omega)\,H_{\mathrm{r}}\right]\,\cos(\hat{\lambda}_m\,x)\left[\hat{\gamma}_m^2(\omega)-\omega^2\right] \\ & + B'_{m,j}(\omega)\,\tilde{\chi}_m(\omega)\,\cosh\left[\tilde{\kappa}_m(\omega)\,H_{\mathrm{r}}\right]\,\sin(\tilde{\lambda}_m\,x)\left[\tilde{\gamma}_m^2(\omega)-\omega^2\right]\Big\} = -g\,\frac{\partial\bar{p}_{\mathrm{I},j}}{\partial y}(x,H_{\mathrm{r}},\omega)\end{aligned} \quad \text{(B6)}$$

where the derivatives $\dfrac{\partial\bar{p}_{I,0}}{\partial y}$ and $\dfrac{\partial\bar{p}_{I,j}}{\partial y}$ can be determined using Eqs. (18) and (19), respectively, the functions $\hat{\gamma}_m$ and $\tilde{\gamma}_m$ are given by Eq. (25), and the parameters $\hat{\chi}_m$ and $\tilde{\chi}_m$ are defined by Eq. (26).

Multiplying Eqs.(B5) and (B6) by $\cos(\hat{\lambda}_m\,x)$ and $\sin(\tilde{\lambda}_m\,x)$, integrating over reservoir length $2b_{\mathrm{r}}$ and using orthogonality properties of trigonometric functions yields the following expression for coefficients $B_{m,0}(\omega)$, $B'_{m,0}(\omega)$, $B_{m,j}(\omega)$ and $B'_{m,j}(\omega)$, $m=1\ldots m_{\mathrm{r}}$, $j=1\ldots m_{\mathrm{s}}$

$$B_{m,\ell}(\omega) = \sum_{n=1}^{m_{\mathrm{r}}} \frac{2\times(-1)^{m+n}\,\rho_{\mathrm{r}} g H_{\mathrm{r}}\,\lambda_n^3(\omega)[I^+_{\ell,n}(\omega) - I^-_{\ell,n}(\omega)]}{b_{\mathrm{r}}\,\beta_n(\omega)\,\hat{\chi}_m(\omega)\left[\kappa_n^2(\omega)+\hat{\lambda}_m^2(\omega)\right]\left[\hat{\gamma}_m^2(\omega)-\omega^2\right]\,\cosh[\hat{\kappa}_m(\omega)\,H_{\mathrm{r}}]}; \qquad \ell=0,j \quad \text{(B7)}$$

$$B'_{m,\ell}(\omega) = \sum_{n=1}^{m_{\mathrm{r}}} \frac{-2\times(-1)^{m+n}\,\rho_{\mathrm{r}} g H_{\mathrm{r}}\,\lambda_n^3(\omega)[I^+_{\ell,n}(\omega) + I^-_{\ell,n}(\omega)]}{b_{\mathrm{r}}\,\beta_n(\omega)\,\tilde{\chi}_m(\omega)\left[\kappa_n^2(\omega)+\tilde{\lambda}_m^2(\omega)\right]\left[\tilde{\gamma}_m^2(\omega)-\omega^2\right]\,\cosh[\tilde{\kappa}_m(\omega)\,H_{\mathrm{r}}]}; \qquad \ell=0,j \quad \text{(B8)}$$

References

ACI committee 350. 2006. Seismic design of liquid-containing concrete structures and commentary (ACI 350.3-06).

ADINA Theory and Modeling Guide., 2010. Report ARD 06-7. ADINA R & D, Inc.

Balendra, T., Ang, K.K., Paramasivam, P. Lee, S.V., 1982. Seismic design of flexible cylindrical liquid storage tanks. Earthquake Engineering and Structural Dynamics 10(3), 477–496.

Bouaanani, N., Paultre, P., Proulx, J., 2002. Two-dimensional modelling of ice cover effects for the dynamic analysis of concrete gravity dams. Earthquake Engineering and Structural Dynamics 31, 2083–2102.

Bouaanani, N., Paultre, P., 2005. A new boundary condition for energy radiation in covered reservoirs using BEM. Engineering Analysis with Boundary Elements 29, 903—911.

Bouaanani, N., Lu, F.Y., 2009. Assessment of potential-based fluid finite elements for seismic analysis of dam-reservoir systems. Journal of Computers and Structures 87, 206–224.

Croteau, P., 1983. Dynamic interactions between floating ice and offshore structures. University of California, Berkeley, Calif. Report No. UCB/EERC-83/06.

Chopra, A.K., 1967. Reservoir-dam interaction during earthquake. Bull. Seismological Soc. of America 57, 675–687.

Chopra, A.K., 1968. Earthquake behavior of reservoir-dam systems. Journal of the Eng. Mech. Div., ASCE 94, 1475–1500.

Chopra, A.K., 1970. Earthquake response of concrete gravity dams. Journal of the Eng. Mech. Div., ASCE 96, 443–454.

Cammaert, A.B., Muggeridge, D.B., 1988. Ice interaction with offshore structures. Van Nostrand Reinhold, New York.

Everstine, G.C., 1981. A symmetric potential formulation for fluid-structure interaction. Journal of Sound and Vibration 79(1), 157–160.

Fenves, G., Chopra, A.K., 1984. Earthquake analysis and response of concrete gravity dams. Earthquake engineering research center.

Fisher, F.D., Rammerstorfer, F.G., 1999. A refined analysis of sloshing effects in seismically excited tanks. International Journal of Pressure Vessels and Piping 76, 693–709.

Ghaemmaghami, A.R., Kianoush, M.R., 2010. Effect of wall flexibility on dynamic response of concrete rectangular liquid storage tanks under horizontal and vertical ground motions 136(4), 441–451.

J. Struct. Eng., 136(4), 441–451.

Gupta, R.K., Hutchinson, G.L., 1990. Effects of wall flexibility on the dynamic response of liquid storage tanks. Engineering Structures 13, 253–267.

Haroun, M.A., Housner, G.W., 1982. Complications in free vibration analysis of tanks. Proc., ASCE Engineering Mechanics Division 108(5), 801–818.

Haroun, M.A., 1980. Dynamic analyses of liquid storage tanks. EERL80-04, Earthquake Engineering Research Laboratory, California Institute of Technology.

Hall, J.F. (ed)., 1995. Northridge Earthquake of January 17, 1994: Reconnaissance Report. Earthquake Spectra, Supplement C to Volume 11, Earthquake Engineering Research Institute, Oakland, CA.

Hanson, R.D., 1973. Behavior of storage tanks, the great Alaska earthquake of 1964. Proc., National Academy of Science, Washington, D.C., 331–339.

Haroun, M.A., 1983. Vibration studies and tests of liquid storage tanks. Earthquake Engineering and Structural Dynamics 11(2), 179–206.

Housner, G.W., 1957. Dynamic pressures on accelerated fluid containers. Bulletin of the Seismological Society of America 47, 15–35.

Housner, G.W., 1963. The dynamic behavior of water tanks. Bulletin of the seismological society of america 53(2), 381–387.

Haroun, M.A., Housner, G.W., 1981a. Seismic design of liquid storage tanks. Journal of Techniqcal Council of ASCE 107, 191–207.

Haroun, M.A., Housner, G.W., 1981b. Earthquake response of deformable liquid storage tanks. Journal of Applied Mechanics 48(2), 411–418.

Jacobsen, L.S., 1949. Impulsive hydrodynamics of fluid inside a cylindrical tank and of fluid surrounding a cylindrical pier. Bulletin of the Seismological Society of America 39(3), 189–204.

Jacobsen, L.S., Ayre, R.S., 1951. Hydrodynamic experiments with rigid cylindrical tnaks subjected to transient motions. Bulletin of the Seismological Society of America 41, 313–346.

Kana, D.D., 1979. Seismic response of flexible cylindrical liquid storage tanks. Nuclear Engineering and Design 52(1), 185–199.

Kiyokawa, T., Inada, H., 1989. Hydrodynamic forces acting on axisymmetric bodies immersed in ice covered sea during earthquakes. Proceedings of 8th International Conference on Offshore Mechanics and Arctic Engineering, The Hague, The Netherlands, 19-23 March 1989. American Society of Mechanical Engineers, New York, 153–159.

Koketsu, K., Hayatama, K., Furumura, T., Ikegami, Y., Akiyama, S., 2005. Damaging long-period ground motions from the 2003 Mw 8.3 Tokachi-Oki, Japan earthquake. Seismological Research Letters 76(1), 58–64.

Krausmann, E., Renni, E., Campedel, M. and Cozzani, V., 2011. Indistrial accidents triggered by earthquakes, floods and lightening: lessons learned from a database analysis. Natural Hazards 59, 285–300.

Malhotra, P.K., Norwood, M.A., Wieland, M., 2000. Simple procedure for seismic analysis of liquid-storage tanks. IABSE Structural Engineering International 3, 197–201.

Martel, C., Nicolas, J.A., Vega, J.M., 1998. Surface-wave damping in a brinmful circular cylinder, J. Fluid Mech. 360, 213–228.

Miura, F., Nozawa, I., Sakaki, N., Hirano, K., 1988. Dynamic stability of an offshore structure surrounded by thick ice during strong earthquake motions. Proceedings of the 9th World Conference on Earthquake Engineering, Tokyo-Kyoto, Japan, August 1988. Japan Association for earthquake Disaster Prevention, Yokyo, Japan. 465–470.

Paultre, P., Proulx, J., and Carbonneau, C. 2002. An experimental evaluation of ice cover effects on the dynamic behaviour of a concrete gravity dam. Earthquake Engineering and Structural Dynamics 31, 2067—2082.

Scarsi, G., 1971. Natural frequencies of viscous liquids in rectangular tanks, Meccanica 6(4), 223–234.

Steinberg, L.J., Cruz, A.M., 2004. When natural and technological disasters collide: Lessons from the Turkey earthquake of August 17, 1999. Natural Hazards Review 5(3), 121–130.

Steinbrugge, K. V., Flores, R., 1963. The Chilean earthquakes of May, 1960: A structural engineering viewpoint. Bulletin of the Seismological Society of America 53(2), 225–307.

Sun, K., 1993. Effects of ice layer on hydrodynamic pressure of structures. ASCE Journal of Cold Regions Engineers 7(3), 63–76.

US Army Corsp of Engineers, 2002. Ice Engineering - Engineer Manual 1110-2-1612. US Army Corps of Engineers, Washington DC. 30 October 2002

Veletsos, A.S., Tang, Y., 1990. Soil-structure interaction effects for laterally excited liquid-storage tanks. Earthquake Engrg. Struct. Dyn. 19, 473–496.

Veletsos, A.S., 1974. Seismic effects in flexible liquid storage tanks. Proc. of Fifth World Conf. on Earthquake Eng., 630–639.

Veletsos, A.S., Yang, J.Y., 1976. Dynamics of fixed-base liquid storage tanks. US-Japan Seminar for Earthquake Engineering Research, Tokyo, Japan, 317–341.

Veletsos, A.S., Yang, J.Y., 1977. Earthquake response of liquid storage tanks. Proc. Second EMD Specialty Conference, ASCE, Raleigh, NC, 1–24.

Weitz, M., Keller, J., 1950. Reflection of water waves from foating ice in water of finite depth. Communications on Pure and Applied Mathematics 3:305-–318.

Werner, P.W., Sundquit, K.J., 1949. On hydrodynamic earthquake effects. Transactions of American Geophysical Union 30(5), 636–657.

Westergaard, H.M.,1933. Water pressures on dams during earthquakes. Transactions, ASCE 98, 418–472.

List of figures

Fig. 1: General geometry of the studied ice-water-structure systems.

Fig. 2: Sub-structuring approach: (a) Containing structure and ice-added mass; (b) reservoir model.

Fig. 3: Geometry of the wall-water system studied in the numerical example.

Fig. 4: Numerical models: (a) Analytical model of the fluid domain and finite element model of the dry containing structure; (b) Coupled fluid-structure interaction finite element model.

Fig. 5: First four mode shapes and corresponding frequencies and effective modal masses of the empty wall-water-ice system: (a) Walls without ice-added mass effects; (b) Walls with ice-added mass effect.

Fig. 6: Frequency response of nondimensionalized hydrodynamic pressures and displacements of the asymmetric wall-water system: (a) Hydrodynamic pressures without ice cover; (b) Hydrodynamic pressures with ice cover; (c) Horizontal displacements without ice cover; (d) Horizontal displacements with ice cover; (e) Vertical displacement of reservoir free surface; (f) Vertical displacement of ice-covered reservoir surface.

Fig. 7: Nondimensionalized hydrodynamic pressure profiles on the walls of the of the asymmetric wall-water system: (a) Convective hydrodynamic pressures without ice cover; (b) Impulsive hydrodynamic pressures without ice cover; (c) Convective hydrodynamic pressures with ice cover; (d) Impulsive hydrodynamic pressures with ice cover.

Fig. 8: Horizontal acceleration component of Imperial Valley earthquake (1940) at El Centro.

Fig. 9: Time-history response of the asymmetric wall-water system without ice: (a) Nondimensionalized displacement at point C; (b) Nondimensionalized displacement at point C'; (c) Nondimensionalized shear force at section A; (d) Nondimensionalized shear force at section A'; (e) Nondimensionalized vertical displacement of water at point B; (f) Nondimensionalized vertical displacement of water at point B'.

Fig. 10: Time-history response of the asymmetric wall-water system with ice: (a) Nondimensionalized displacement at point C; (b) Nondimensionalized displacement at point C'; (c) Nondimensionalized shear force at section A; (d) Nondimensionalized shear force at section A'; (e) Nondimensionalized vertical displacement of water at point B; (f) Nondimensionalized vertical displacement of water at point B'.

Fig. 11: Time-history responses of the symmetric and asymmetric wall-water systems: (a) Nondimensionalized displacement at point C without ice; (b) Nondimensionalized displacement at point C with ice; (c) Nondimensionalized vertical displacement of water at point B without ice; (d) Nondimensionalized vertical displacement of water at point B with ice; (e) Nondimensionalized vertical displacement of water at point B' without ice; (f) Nondimensionalized vertical displacement of water at point B' with ice.

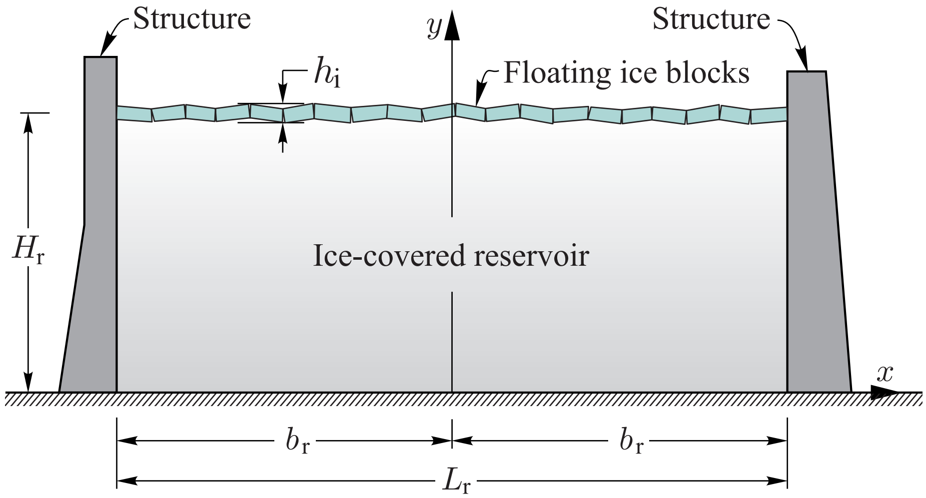

Figure 1. General geometry of the studied ice-water-structure systems.

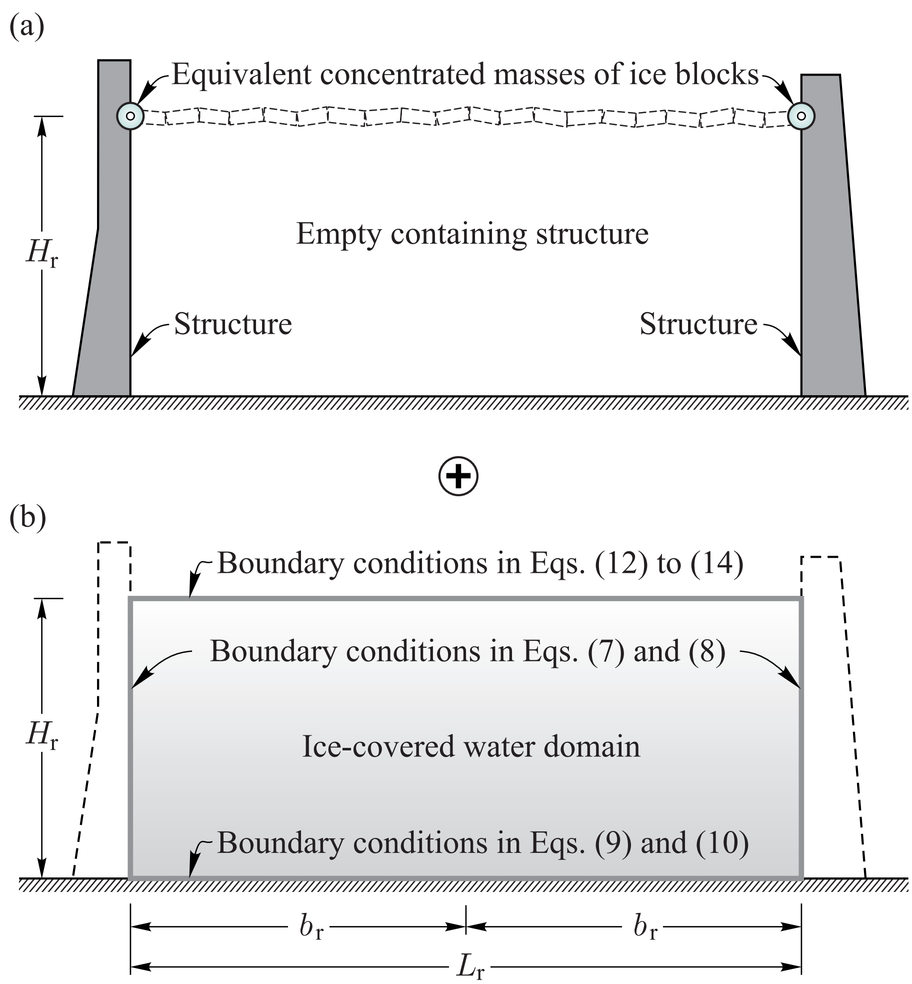

Figure 2. Sub-structuring approach: (a) Containing structure and ice-added mass; (b) reservoir model.

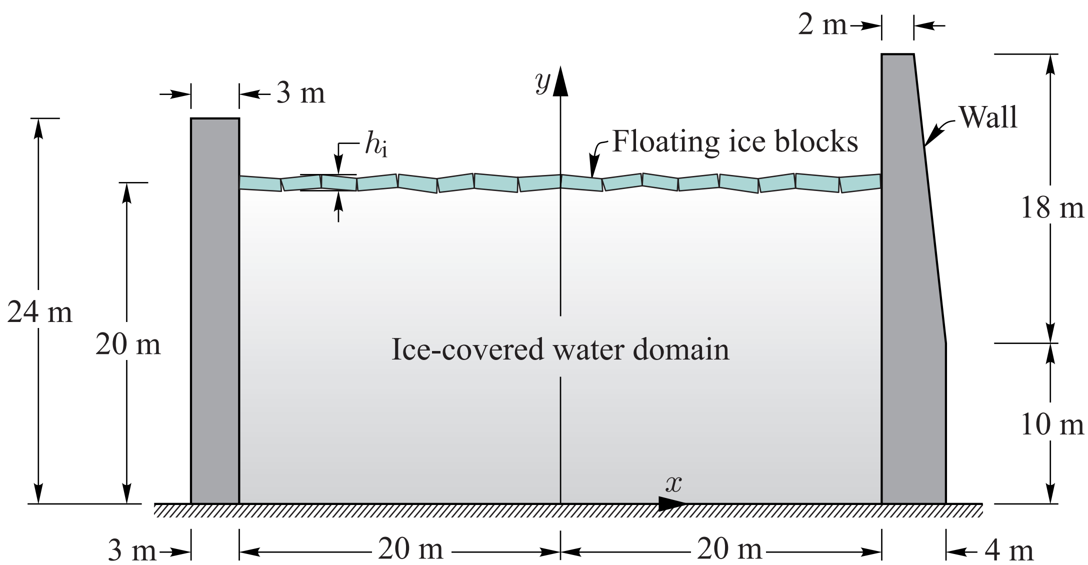

Figure 3. Geometry of the wall-water system studied in the numerical example.

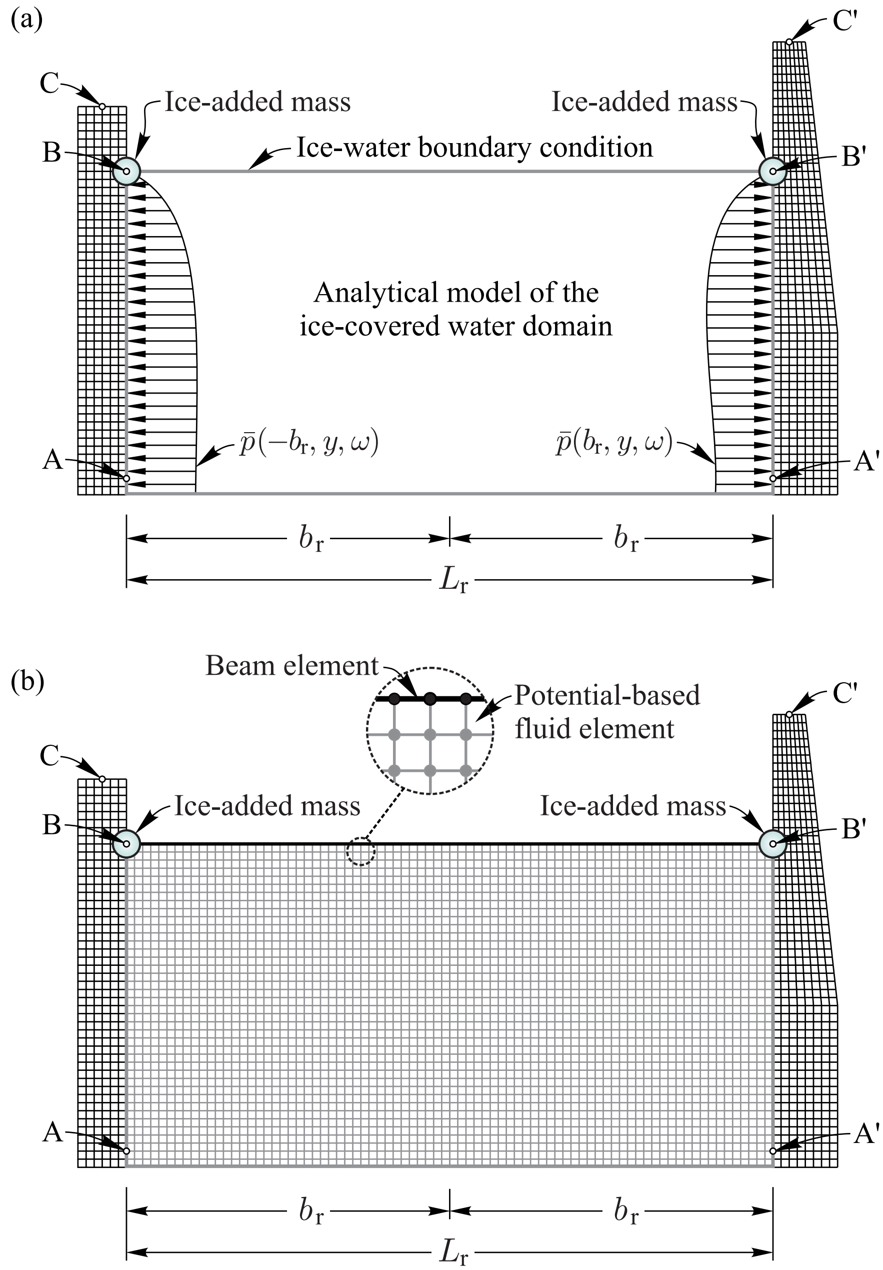

Figure 4. Numerical models: (a) Analytical model of the fluid domain and finite element model of the dry containing structure; (b) Coupled fluid-structure interaction finite element model.

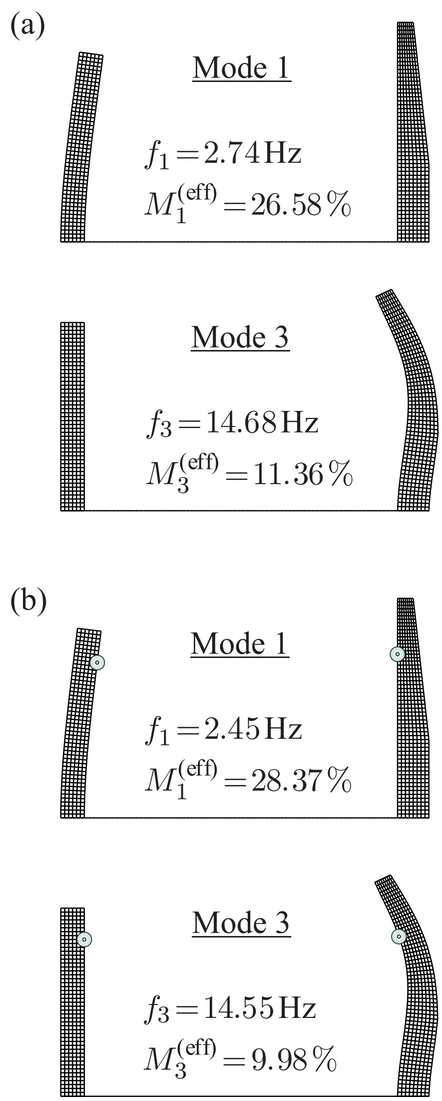

Figure 5. First four mode shapes and corresponding frequencies and effective modal masses of the empty container: (a) Walls without ice-added mass effect; (b) Walls with ice-added mass effect.

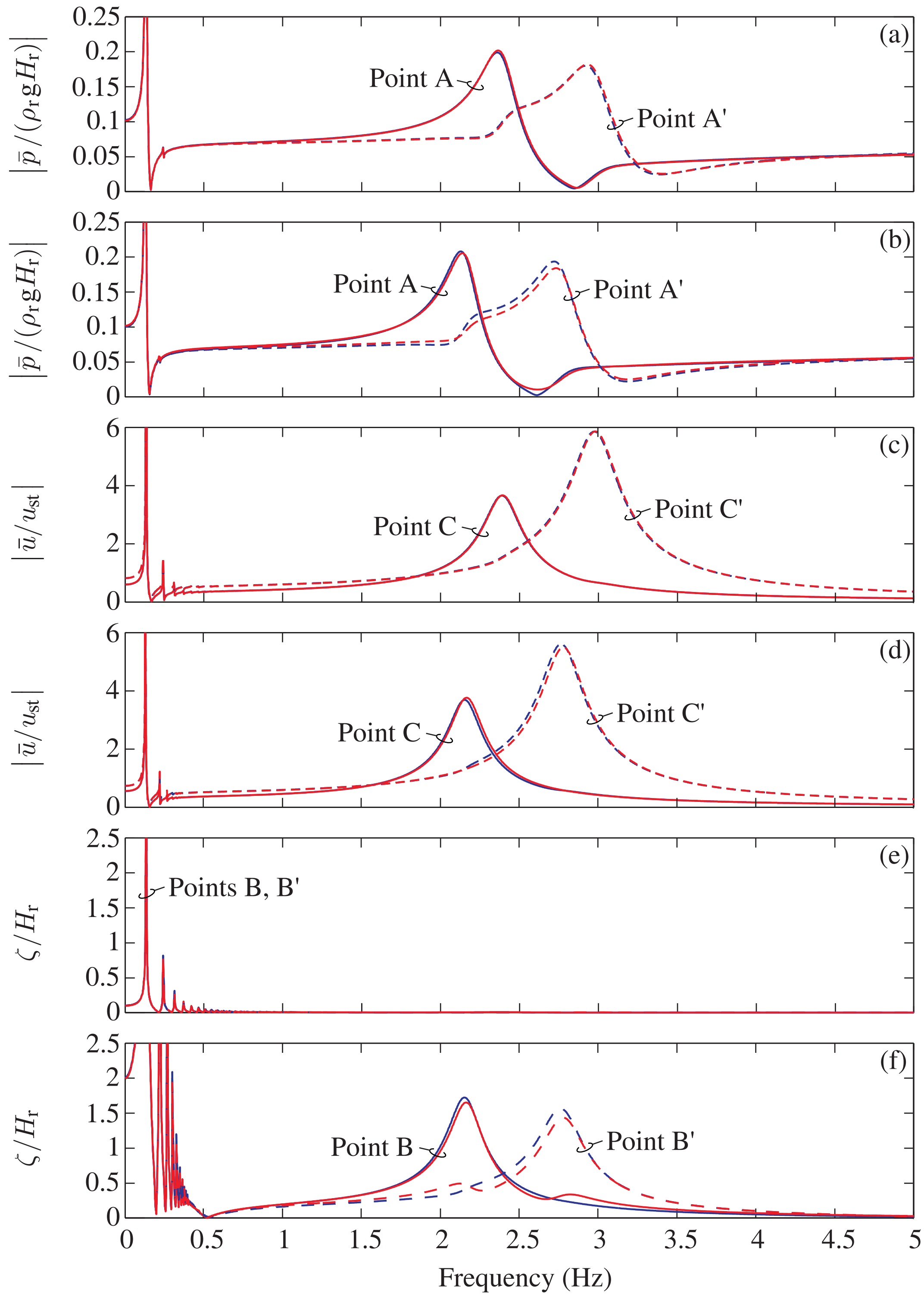

Figure 6. Frequency response of nondimensionalized hydrodynamic pressures and displacements of the asymmetric wall-water system: (a) Hydrodynamic pressures without ice cover; (b) Hydrodynamic pressures with ice cover; (c) Horizontal displacements without ice cover; (d) Horizontal displacements with ice cover; (e) Vertical displacement at reservoir free surface; (f) Vertical displacement at ice-covered reservoir surface. ▬ Finite element solution; ▬ Proposed solution.

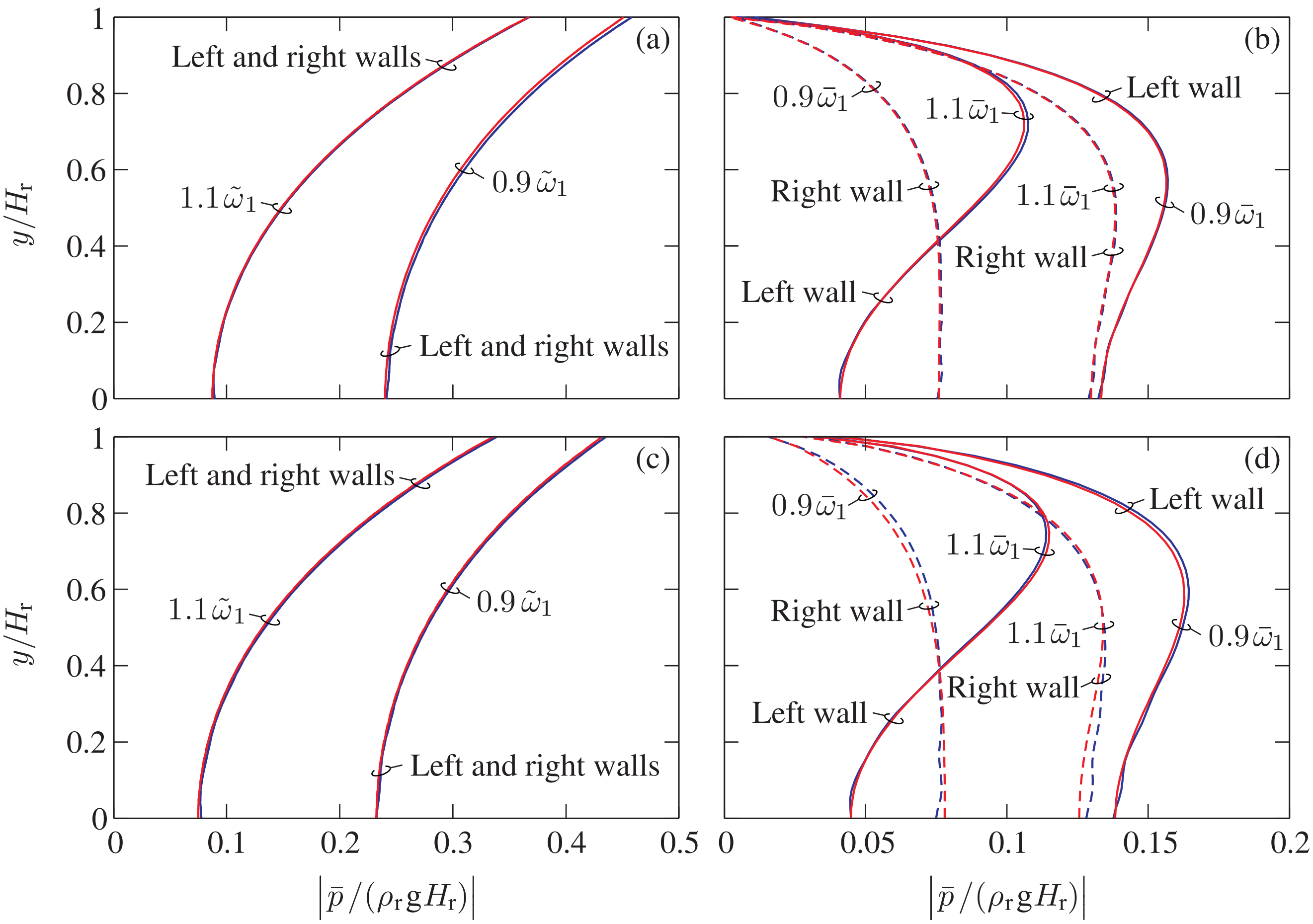

Figure 7. Nondimensionalized hydrodynamic pressure profiles on the walls of the asymmetric wall-water system: (a) Convective hydrodynamic pressures without ice cover; (b) Impulsive hydrodynamic pressures without ice cover; (c) Convective hydrodynamic pressures with ice cover; (d) Impulsive hydrodynamic pressures with ice cover. Finite element solution; Proposed solution.

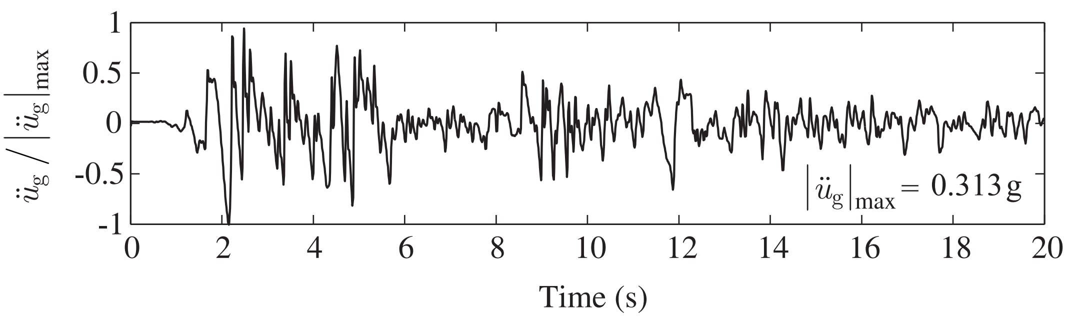

Figure 8. First 20 s of the horizontal acceleration component of Imperial Valley earthquake (1940) at El Centro.

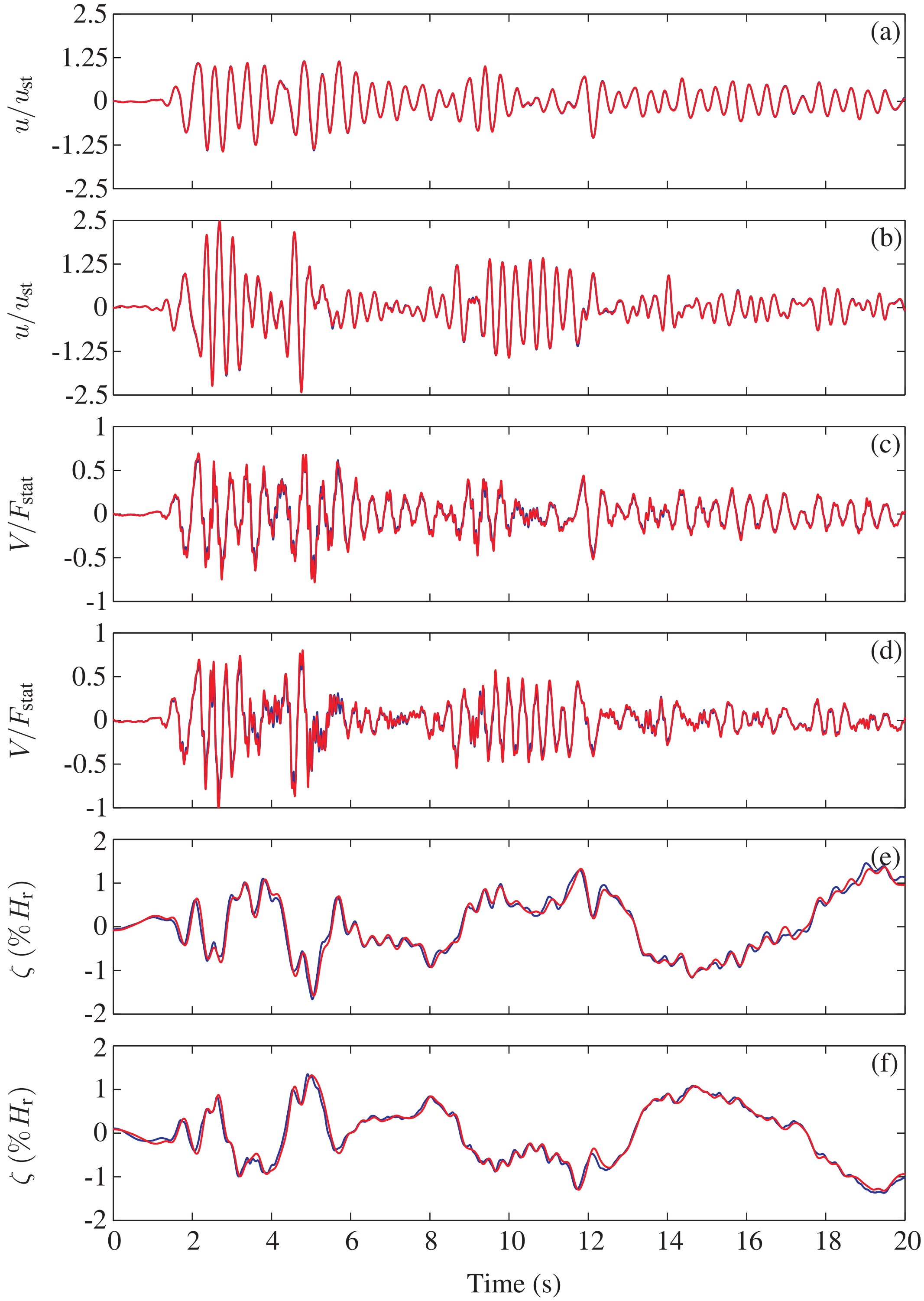

Figure 9. Time-history response of the asymmetric wall-water system without ice: (a) Nondimensionalized displacement at point C; (b) Nondimensionalized displacement at point C'; (c) Nondimensionalized shear force at section A; (d) Nondimensionalized shear force at section A'; (e) Nondimensionalized vertical displacement of water at point B; (f) Nondimensionalized vertical displacement of water at point B'. —— Finite element solution; —— Proposed solution.

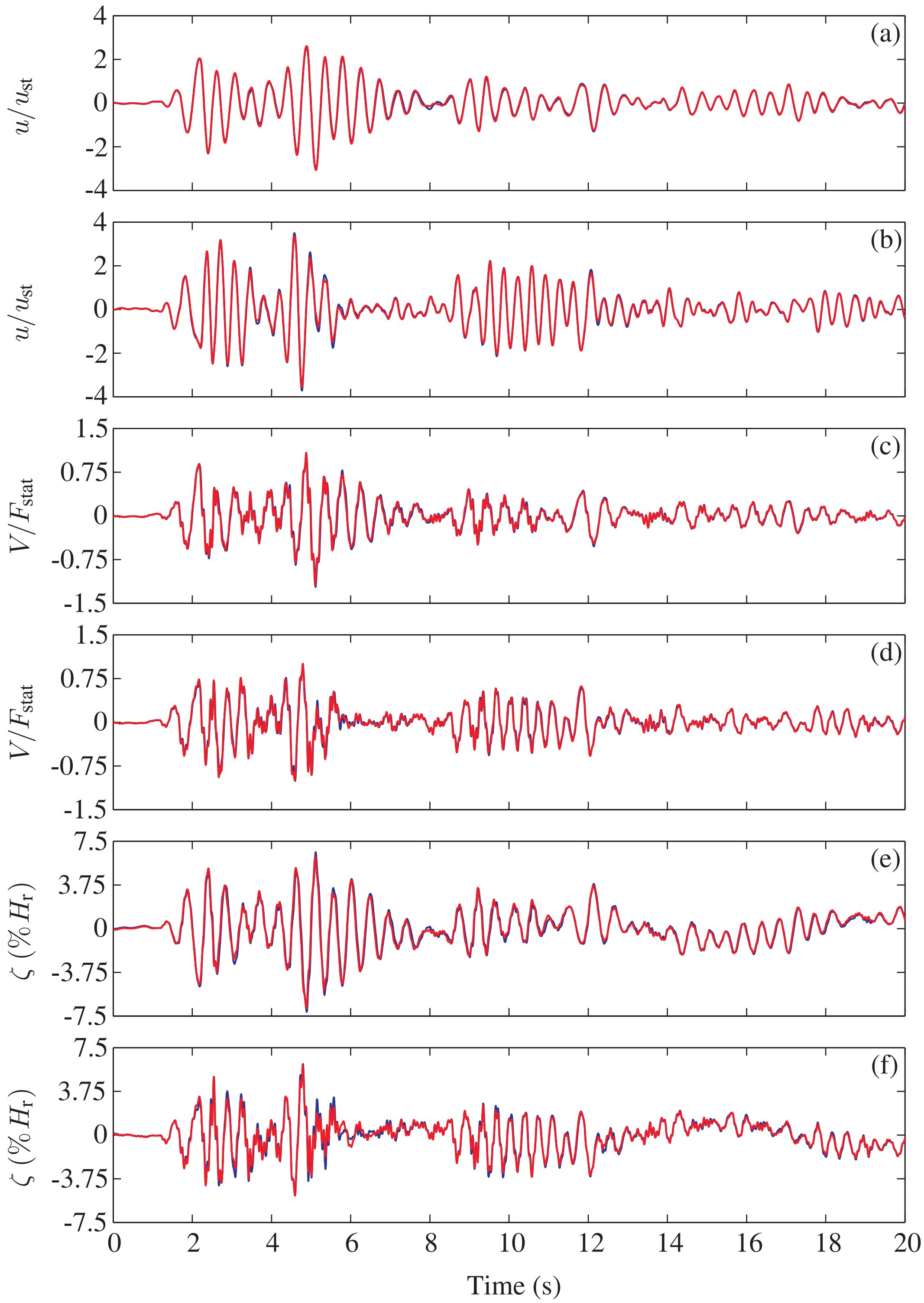

Figure 10. Time-history response of the asymmetric wall-water system with ice: (a) Nondimensionalized displacement at point C; (b) Nondimensionalized displacement at point C'; (c) Nondimensionalized shear force at section A; (d) Nondimensionalized shear force at section A'; (e) Nondimensionalized vertical displacement of water at point B; (f) Nondimensionalized vertical displacement of water at point B'. —— Finite element solution; —— Proposed solution.

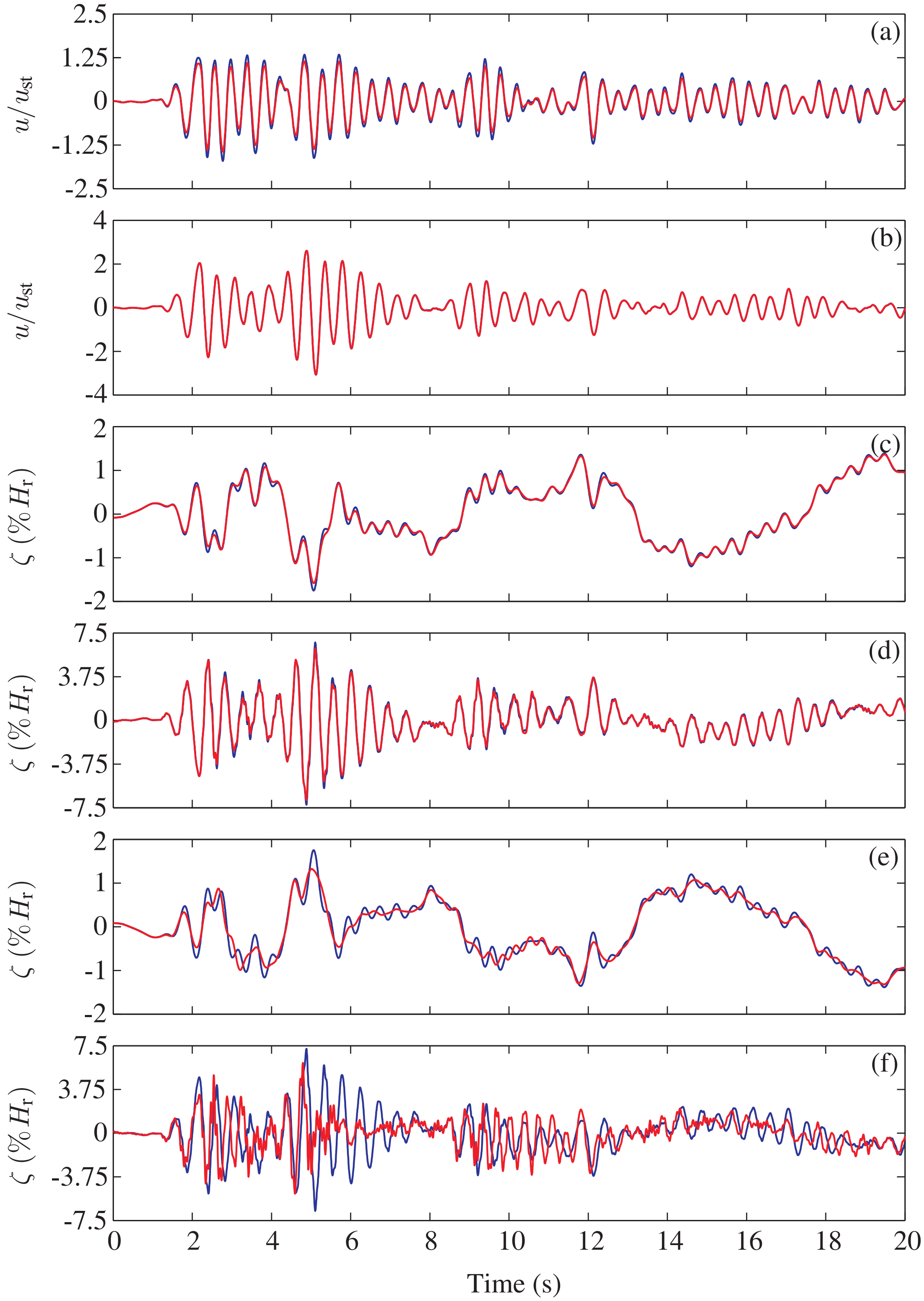

Figure 11. Time-history responses of the symmetric and asymmetric wall-water systems: (a) Nondimensionalized displacement at point C without ice; (b) Nondimensionalized displacement at point C with ice; (c) Nondimensionalized vertical displacement of water at point B without ice; (d) Nondimensionalized vertical displacement of water at point B with ice; (e) Nondimensionalized vertical displacement of water at point B' without ice; (f) Nondimensionalized vertical displacement of water at point B' with ice. —— Symmetric structure; —— Asymmetric structure.